Enhanced Photoconversion Efficiency in Cesium-Antimony-Halide Perovskite Derivatives by Tuning Crystallographic Dimensionality

Yueheng Peng[a,1], Fengzhu Li[a], Yan Wang[a], Yachen Li[a], Robert L. Z. Hoye[b], Linrun Feng[c], Kai Xia[a], Vincenzo Pecunia[a,1,*]

[a]*Institute of Functional Nano & Soft Materials (FUNSOM), Jiangsu Key Laboratory for Carbon-Based Functional Materials & Devices, Soochow University, 199 Ren'ai Road, Suzhou, 215123, Jiangsu, PR China.*

[b]*Department of Materials, Imperial College London, Exhibition Road, London SW7 2AZ, United Kingdom.*

[c]*Wuhan LinkZill Technology Co., Ltd., Modern Optics Valley World Trade Center, 70 Guanggu Road, Wuhan, 430073, Hubei, China.*

* Corresponding authors.

E-mail address: vp293@suda.edu.cn (V. Pecunia)

[1] These authors contributed equally to this work.

Abstract

Lead-based perovskites have reached prominence in optoelectronic and photovoltaic research, yet their toxicity has prompted the search for alternative lead-free compounds. All-inorganic antimony-/bismuth-halide perovskite derivatives have been identified as a promising class of materials. Despite attractive bulk optoelectronic properties, their optoelectronic device performance has been lagging behind. Here we examine one of their most promising embodiments, the all-inorganic cesium-antimony-halide system. Through solution-based halide mixing, we achieve its structural conversion from a zero-dimensional to a layered phase at processing temperatures <150 °C, i.e., much lower than those relied upon in the prior literature ($\geq$ 230 °C) of all-inorganic cesium-antimony halides. In order to evaluate the technological significance of such finding, we integrate our layered films into a sandwich-type device structure, and characterize their external quantum efficiency and photovoltaic behavior. We find that the structural conversion leads to a considerable enhancement of the optoelectronic device performance. Additionally, photocurrent-power characterization and Hall effect measurements reveal that this performance enhancement is brought about by an improvement in charge carrier transport, which can be exploited due to the unoriented nature of our low-temperature-processed layered films. Such performance boost and mechanistic insight constitute an important step in realizing the full potential of these (and related) compounds for their application in lead-free optoelectronic and photovoltaic devices, e.g., for top-cell in tandem photovoltaics, indoor photovoltaics, and photodetection.

1. Introduction

In recent years, lead-halide perovskites have emerged as particularly promising semiconductors for optoelectronic applications [1–10]. For instance, in photovoltaics, power conversion efficiencies (PCEs) now surpassing the 25% threshold have been achieved [11]. However, toxicity concerns associated with the lead content [12] of lead-halide perovskites have hindered their large-scale commercialization. Consequently, considerable efforts have been put forward in developing perovskites and derivatives with similarly favorable optoelectronic properties but with lead being replaced with less toxic elements [13–16].

A promising approach to lead-free-perovskite optoelectronics has been identified in the substitution of lead with group-VA elements. Their 3+ cations are isoelectronic with Pb^{2+} and have similar ionic radii, thus enabling the formation of perovskite derivatives (in this work we refer to these compounds as perovskites for conciseness, but we stress that they do not necessarily have the perovskite crystal structure) [14,17]. Consequently, antimony-/bismuth-halide perovskites (compounds with formula $A_3M_2X_9$, where A^+ is a monovalent organic or alkali metal cation, M^{3+} is either Sb^{3+} or Bi^{3+}, and X^- is a halide anion) have attracted considerable attention [14,18–24]. This is especially because of their large absorption coefficient ($> 1 \cdot 10^5$ cm^{-1}) and the similarity of their electronic structures to those of lead-halide perovskites [14,21–23]. In particular, antimony-based compounds of this class (A-Sb-Xs in short form) have been found especially appealing in view of their appreciably smaller exciton binding energy (~ 100 meV range) [24] compared to the

2

bismuth-based counterparts (~ 300–400 meV range) [20,23,25], which suggests greater promise for photoconversion purposes [24]. Antimony-based perovskite derivatives typically come in a zero-dimensional (0D) crystal structure, featuring isolated bioctahedral face-sharing $[Sb_2X_9]^{3-}$ clusters (dimer form) [23,24,26] Nonetheless, some of these compounds may form a two-dimensional (2D) structure, consisting of sheets of corner-sharing $[SbX_6]^{3-}$ octahedra (layered form) [23,26,27]. The latter is the case for all-inorganic A-Sb-Xs (i.e., A-Sb-Xs in which A^+ is an inorganic cation) [24,26,28–31]. Indeed, a 2D structure is inherently obtained with $A^+ = Rb^+$ and $A^+ = K^+$, whereas Cs^+ delivers the same through specialized processing (thermal evaporation [26] or treatments at temperatures $\geq$ 230 °C [29,30]).

A 2D structure has been linked to superior charge transport properties, since charges are expected to be more mobile within the octahedral sheets than in a system of isolated dimers [26]. In addition, all-inorganic A-Sb-Xs with a 2D structure have been shown to lead to a lower and quasi-direct optical gap compared to the 0D case [26]. While this all points to their significant photoconversion potential, 2D all-inorganic A-Sb-Xs have yet to match this expectation. For instance, after some initial progress in photovoltaics, their power conversion efficiencies have seemingly reached a saturation point at 1.49% (as achieved in one champion device of layered $Cs_3Sb_2I_9$ grown at a temperature as high as 250 °C) [29]. In fact, this has been the case for a wide range of all-inorganic layered A-Sb-Xs: not only $Cs_3Sb_2I_9$, but also $K_3Sb_2I_9$, $Rb_3Sb_2I_9$, and $Rb_3Sb_2Br_xI_{9-x}$ [24,26,28–31]. Importantly, within the family of two-dimensional all-inorganic A-Sb-Xs, the cesium-based system ($A^+ = Cs^+$) is particularly promising. In fact, it has delivered the highest photovoltaic performance [29]

and also possesses a smaller direct bandgap than the two-dimensional all-inorganic A-Sb-X second-best in performance (i.e., $Rb_3Sb_2I_9$) [26,28–30].

In the broader area of low-dimensional-perovskite optoelectronics, it has been generally established that the crystalline orientation is a key determinant of device performance. For instance, 2D lead-based perovskites give their best photovoltaic efficiency in sandwich-type devices when their octahedral sheets are orthogonal to the substrate [32–34]. Indeed, it is only then that the high charge carrier mobility direction is parallel to the direction of charge extraction in sandwich-type devices. Interestingly, most all-inorganic A-Sb-X photovoltaic studies use oriented films with the octahedral sheets predominantly parallel to the substrate [24,26,28–31]. In addition, within the realm of solution processing, it has been found that the deposition temperatures of low-dimensional perovskites play an important role in conditioning their crystalline orientation [32,35]. With regard to $Cs_3Sb_2I_9$, it is worth noting that solution-based deposition methods have relied on temperatures above 230 °C in order to form a 2D structure rather than a 0D structure [29,30].

Based on these indications and with a focus on the cesium-antimony-halide system (a prominent all-inorganic A-Sb-X), this study aims to further assess and realize the potential of lead-free all-inorganic antimony-based perovskites. This is pursued through the compositional manipulation of $Cs_3Sb_2I_9$ in order to realize its robust and reproducible 0D-to-2D structural conversion while preventing a preferential in-plane orientation. We demonstrate that this can be achieved through a solution-based low-temperature route, which involves the replacement of a fraction of iodine with chlorine, leading to the formation of unoriented films of 2D $Cs_3Sb_2Cl_xI_{9-x}$. To evaluate the significance of this

approach, we also characterize the photoconversion efficiency of devices comprising our compounds. These devices show that the structural conversion leads to a significant performance enhancement, which can be explained in terms of the corresponding charge transport properties.

2. Material and methods

2.1 Materials

All chemicals were used as received and without further purification. CsI (99.999% Alfa Aesar), CsCl (99.9%, Alfa Aesar), SbI$_3$ (99.999%, Sigma-Aldrich), SbCl$_3$ (99.999%, Alfa Aesar), DMSO (dimethylsulfoxide, analytical grade, Beijing Chemical Reagent Co.), DMF (N,N-dimethylfomamide, analytical grade, Beijing Chemical Reagent Co.), toluene (super-dry, Beijing Chemical Reagent Co.), hydriodic acid (HI(*aq*)) (57 wt.% in H$_2$O, 99.95%, Sinopharm), chlorobenzene (CB) (> 99%, J&K), chloroform (anhydrous, J&K), Titanium(IV) Isopropoxide (Sigma-Aldrich), titania paste (18NR-T, Greatcell Solar), poly[N,N'-bis(4-butylphenyl)-N,N'-bisphenylbenzidine] (poly-TPD) (Lumtec), LZ-HTL-1-1 (Linkzill), CYTOP CTL-809M (Asahi Glass AGC Group), n-butyl acetate (anhydrous, Sigma Aldrich), Poly(methyl methacrylate) (PMMA) (M$_W$ ≈ 120 000) (Sigma Aldrich).

2.2 Cs$_3$Sb$_2$Cl$_x$I$_{9-x}$ film deposition

Precursor solutions were prepared by dissolving CsI, SbI$_3$, CsCl, and SbCl$_3$ in different molar ratios (depending on the target compound) in DMSO:DMF (3:1 volume ratio) within a nitrogen-filled glove box. The solutions were stirred overnight at 70°C. After the solutions were cooled down to room temperature, HI(*aq*) (30 μL mL^{-1}) was added 60 min before the solutions were spin-coated. After the solutions were filtered (using polytetrafluoroethylene filters with 0.22 μm pore size), they were spin-coated at 4000 rpm

5

for 30 s. Approximately 20 s into the spin-coating cycle, toluene (100 μL) was dispensed onto the substrate. Finally, an annealing step was carried out on a hotplate set to the specified annealing temperature (100 – 150 °C, with the best performance being achieved at 135 °C) for 30 min. In particular, three different annealing arrangements were employed. In one case, which we refer to as *direct annealing*, the as-coated sample was placed directly on the hotplate. Another arrangement, referred to as *capped annealing*, involved having the as-coated sample turned over onto a glass slide placed on the hotplate. A final arrangement, referred to as *solvent vapor annealing*, involved placing the as-coated sample on the hotplate and within a Petri dish containing 5 μL of DMSO.

2.3 Device fabrication

Glass substrates coated with patterned fluorine-doped tin-oxide (FTO) electrodes (Ying Kou You Xuan Trade Co. Ltd) were sequentially sonicated in a water-based detergent, deionized water, acetone, and isopropanol (5 min each). After they were dried under N_2 flow, the substrates were treated with UV-ozone for 30 min. A compact TiO_2 film (c-TiO_2) was deposited from a precursor solution based on Titanium(IV) Isopropoxide (as per procedure reported in Ref. [36]) and annealed at 450 °C for 45 min. Subsequently, titania paste was spin-coated (at 7000 rpm for 60 s) and annealed at 450 °C for 45 min in order to form a mesoporous TiO_2 (m-TiO_2) layer. The substrates were then transferred to a nitrogen-filled glove box, where the intended perovskite layer was deposited from a 0.3 M precursor solution (see Section 2.2). This was followed by the spin coating of a poly-TPD solution (10 mg mL^{-1} in chloroform) or a LZ-HTL-1-1 solution (10 mg mL^{-1} in chlorobenzene) (at 4000 rpm for 30 s). Finally, 40-nm-thick gold anodes were thermally evaporated in high vacuum, defining a device active area of 7.25 mm^2.

6

2.4 General characterization

X-ray diffraction (XRD) measurements were carried out using a Panalytical Empyrean X-ray diffractometer. Optical transmission measurements were conducted using a PerkinElmer LAMBDA 750 UV/Vis/NIR spectrophotometer. Scanning Electron Microscopy (SEM) and Energy-Dispersive X-ray Spectroscopy (EDS) were conducted using a Zeiss GeminiSEM 500 (10 kV) and an Oxford Xmax 20. Ultraviolet Photoemission Spectroscopy (UPS) measurements were conducted using a Kratos Ultra DLD X-ray/ultraviolet photoelectron spectrometer, which featured a monochromatic He I (21.2 eV) excitation source. Thermal stability was characterized using a Mettler Toledo TGA1 thermogravimetric analysis system.

2.5 Optoelectronic device characterization

External quantum efficiency (EQE) measurements were conducted (in air) using a custom-built setup comprising a monochromated light source (Zolix, Omni-λ2005i), a calibrated power meter assembly (Thorlabs PM200 and Thorlabs S120VC), and a source meter (Keithley 6420). Photovoltaic performance was assessed using a simulated AM 1.5G source (100 mW cm^{-2}, Xenon lamp, Newport). Current-voltage characteristics under illumination were acquired with a Keithley 2400 source meter.

2.6 Stability characterization

Stability characterization was conducted on devices and films comprising $Cs_3Sb_2Cl_3I_6$ layers. In addition to non-encapsulated devices and films fabricated as specified in Sections 2.2 and 2.3, films capped with a 400-nm-thick PMMA film were also considered (PMMA was dissolved in n-butyl acetate at a concentration of 80 mg mL^{-1}, spin coated at 2000rpm for 30s and annealed at 90 °C, with all such steps conducted within an N$_2$-filled glove box).

All samples were kept at a temperature in the range of 20 – 25 °C for the entire duration of the experiment. Some of the samples were stored in an N_2-filled glove box throughout the experiment, except for the time intervals (each approximately 1 hour long) required for testing. Samples stored in air were subjected to a relative humidity in the range of 40 – 100 %. Testing was carried out at discrete times, and involved J-V characterization under simulated AM1.5G illumination (for devices), or XRD and UV-Vis spectrophotometry (for films).

2.7 Hall effect characterization

Glass substrates coated with films of the target compounds (deposited through the same procedure detailed in Section 2.2) were cut to a square size of $1 \cdot 1$ cm^2. Silver paste electrodes with an area of $1 \cdot 1$ mm^2 were deposited at the four corners of the sample in order to realize a van der Pauw device. Hall effect measurements were conducted using an electromagnet-based system (Lakeshore 8404) at room temperature, in air, and in the dark. van der Pauw samples were subjected to a sinusoidally-modulated magnetic field (root-mean-square amplitude of 0.42291 T and modulation frequency of 100 mHz) and to an excitation current in the range of 50 – 500 pA.

2.8 HTL mobility characterization through field-effect charge modulation

Top-gate bottom-contact transistors were fabricated on glass substrates using photolithographically-patterned channel contacts (made of a 2-nm-thick Cr layer and a 20-nm-thick Au layer, and defining a channel width of 1000 μm and channel length of 20 μm) following a standard procedure reported in the literature [37]. Subsequently, poly-TPD was dissolved in chloroform (10 mg mL^{-1}) and LZ-HTL-1-1 in chlorobenzene (20 mg mL^{-1}). Hole transport layers (HTLs) were deposited by spin coating and subsequently annealed at

100 °C for 5 min (in a nitrogen-filled glove box). A 620-nm-thick CYTOP film was then spin-coated on the HTL film and annealed at 90 °C for 20 min. Finally, 50-nm-thick Al gate electrodes were defined by thermal evaporation through a shadow mask.

3. Results and discussion

The $Cs_3Sb_2I_9$ dimer phase has been rationalized as resulting from the rotation of adjacent $[SbI_6]^{3-}$ octahedra around their bridge iodine and into $[Sb_2I_9]^{3-}$ bioctahedra, which allows Cs^+ cations to be accommodated [38]. Building on this insight and encouraged by recent results on related bismuth-based and organic-inorganic antimony-based compounds [39–42], we hypothesized that the formation of the dimer phase of $Cs_3Sb_2I_9$ could be prevented by replacing some of the bulky iodine ($r_{I^-} = 220\ pm$) with smaller halides. This was in consideration that shorter Sb-X bonds (where X is a halide) may leave more space for cesium cations ($r_{Cs^+} = 167\ pm$) to fit between neighboring corner-sharing $[SbX_6]^{3-}$ octahedra (as per layered phase). Following this lead, we explored the possibility of converting $Cs_3Sb_2I_9$ to its layered phase through the solution-based fractional substitution of iodine with chlorine ($r_{Cl^-} = 181\ pm$), thus targeting the synthesis of compounds with the formula $Cs_3Sb_2Cl_xI_{9-x}$. We reasoned that such a compositional engineering approach to the structural conversion of $Cs_3Sb_2I_9$ would not require the high-processing temperatures of the approaches explored to date, thus potentially allowing more flexibility in terms of crystalline orientation of the resulting compounds. Incidentally, we note that the concept outlined here does not relate to a recent work in which layered $Cs_3Sb_2I_9$ was prepared at high temperature (230 °C) with HCl as an additive in the precursor solution, but with no chlorine left in the final films [30]. The synthesis of $Cs_3Sb_2Cl_xI_{9-x}$ ($Cs_3Sb_2I_9$ serving as the reference) was pursued by mixing powders of SbI_3, $SbCl_3$, CsI, and CsCl with the

9

appropriate molar ratios and by dissolving them in suitable solvents. In order to overcome the poor solubility of CsI and CsCl in common organic solvents (which had previously been reported to prevent the synthesis of $Cs_3Sb_2Cl_xI_{9-x}$ altogether [42]), we employed a DMSO:DMF solvent mixture in which we introduced a small amount of hydroiodic acid (HI(aq)) (30 µL per mL of precursor solution). This led to a considerable solubility improvement, which enabled the synthesis and deposition of $Cs_3Sb_2Cl_xI_{9-x}$ films. However, a solution could not be obtained for high chlorine content ($x > 4$). Consequently, we focused our synthetic efforts on target compounds $Cs_3Sb_2Cl_xI_{9-x}$ with $x \leq 4$. A standard one-step antisolvent spin-coating procedure was used to deposit thin films of the target compounds (**Fig. 1**a). This was followed by annealing at a temperature T_{anneal} in the range of 100 – 150 °C.

In order to enhance the film quality, we carried out an extensive optimization of the annealing step. This was necessary because of the poor morphology that was obtained when antisolvent spin-coating was followed by hotplate annealing (direct annealing; DA in short form) (**Fig. 1**a; see Section 2.2 for details). Indeed, such $Cs_3Sb_2Cl_xI_{9-x}$ films had an amorphous-like appearance (**Fig. 1**b), suggesting an incomplete crystallization of the precursors (we note that, when imaging DA samples with SEM, it was necessary to limit the magnification in order to prevent significant damage from the electron beam). Based on these indications, we considered reducing the solvent evaporation rate by carrying out the hotplate annealing step with the sample turned over onto a glass slide (capped annealing; CA in short form) (**Fig. 1**a; see Section 2.2 for details). This was with the aim of having residual solvent in the film for longer, potentially aiding crystallization. Indeed, this resulted in a significant improvement in microstructure, with apparent grain size

around 100 nm (**Fig. 1**b). Hypothesizing that a larger amount of solvent vapor could enhance crystallization and microstructure further, we then attempted a solvent vapor annealing (SVA) approach. This was carried out with the same arrangement as direct annealing, except that the sample was enclosed in a glass container and had a few droplets
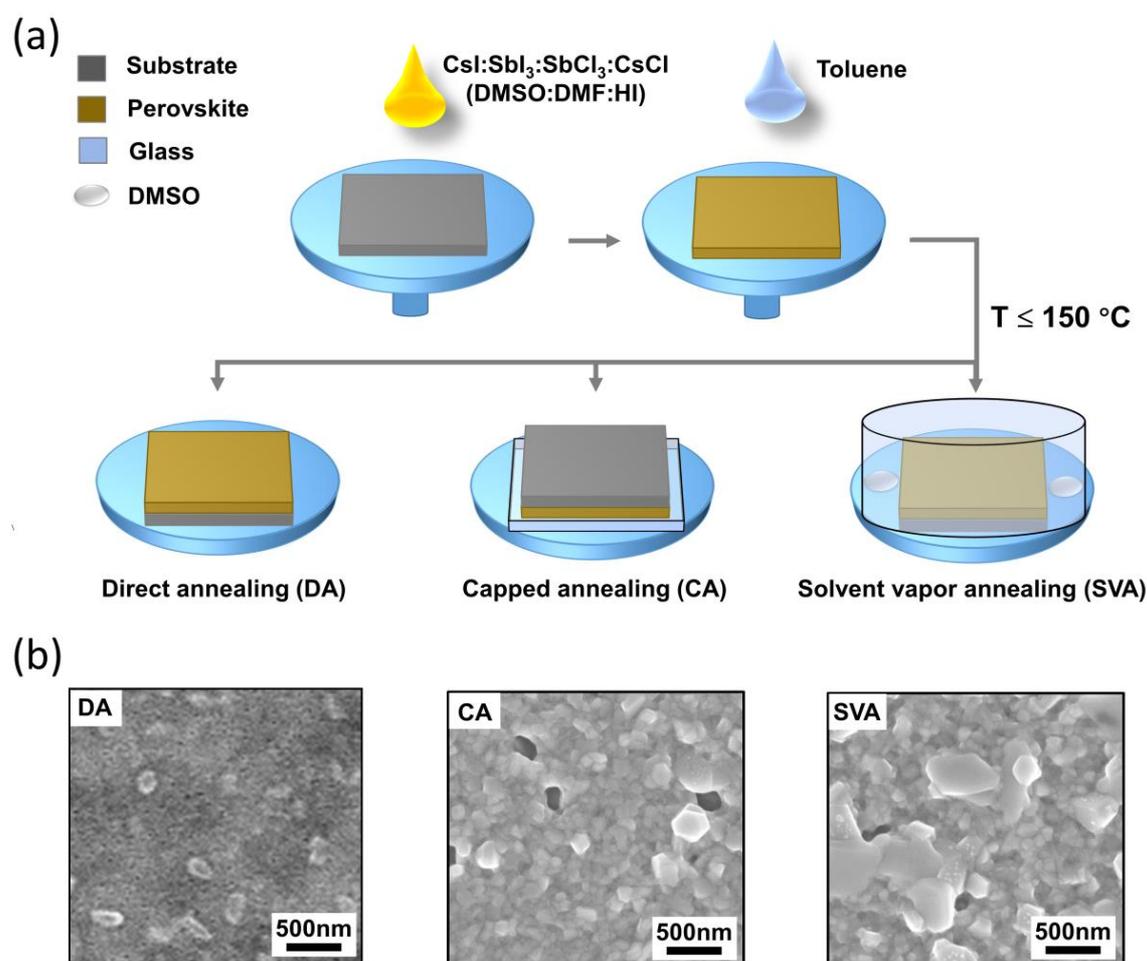

Fig. 1. Synthesis and deposition of $Cs_3Sb_2Cl_xI_{9-x}$ thin films. (a) Process flow. (b) Representative SEM images of films of $Cs_3Sb_2Cl_3I_6$ (on compact TiO_2) obtained through direct annealing (left), capped annealing (middle), and solvent vapor annealing (right).
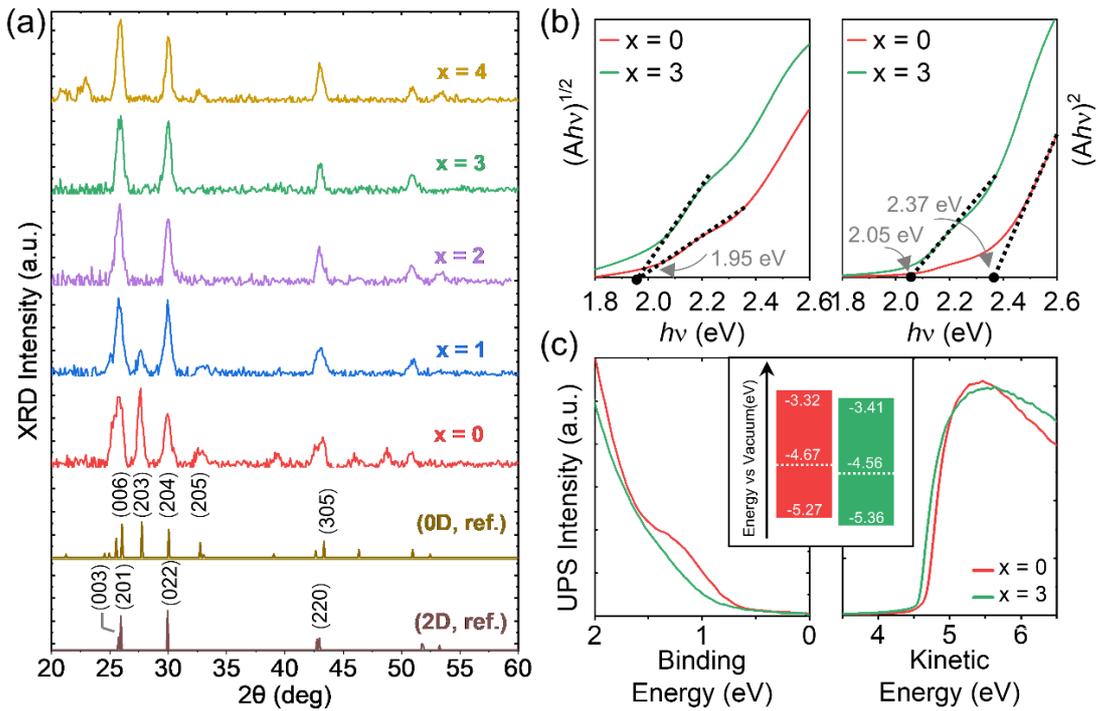
Fig. 2. (a) Measured XRD patterns from $Cs_3Sb_2Cl_xI_{9-x}$ thin films ($x = 0 – 4$), along with reference patterns for 0D and 2D $Cs_3Sb_2I_9$ (ICSD collection codes 001447 and 084990) [38,43]. (b) Tauc plots of $Cs_3Sb_2I_9$ (0D) and $Cs_3Sb_2Cl_3I_6$ (2D). (c) UPS intensity (valence band states (left) and He I secondary electron cutoff (right)) from $Cs_3Sb_2I_9$ (0D) and $Cs_3Sb_2Cl_3I_6$ (2D) films. Inset: energy levels combining the findings from UPS and UV-Vis measurements, assuming negligible excitonic effects.

of DMSO in its vicinity (**Fig. 1**a; see Section 2.2 for details). We found that this enabled

further microstructural improvement, allowing the formation of large (> 600 nm) grain-

like domains interspersed within an otherwise similar domain matrix (**Fig. 1**b). A similar

microstructural improvement was also achieved on a mesoporous substrate (mesoporous

titanium oxide; m-TiO₂ in short form), yet with smaller grain size and lower coverage (**Fig.**

S1). We note that the microstructural improvement obtained with CA and SVA was asso-

ciated with an increase in the amount of solvent present during the annealing step. This can

be rationalized in terms of an enhancement of the grain growth rate mediated by a reduction

in the supersaturation level during the annealing step [44,45]. Based on the aforementioned

trend in grain size, the brighter regions in the images in **Fig. 1**b can be traced to the edge effect customarily observed with SEM, which is often associated with raised crystalline domains of particular tilt angles and/or particular crystalline orientations [46,47]. In view of their generally superior morphology, we considered solvent-vapor-annealed $Cs_3Sb_2Cl_xI_{9-x}$ films for all subsequent characterization.

To evaluate the structural impact of Cl incorporation, we conducted a systematic X-ray diffraction (XRD) study on thin films with the target formula $Cs_3Sb_2Cl_xI_{9-x}$ ($x = 0 – 4$ as per precursor mixing ratios). The resulting XRD patterns are shown in **Fig. 2**a, along with reference patterns of $Cs_3Sb_2I_9$ in its dimer and layered phases [38,43] (see also **Fig. S2** for reference patterns in semilogarithmic scale). Patterns from ternary $Cs_3Sb_2I_9$ films were consistent with the literature on dimer-phase $Cs_3Sb_2I_9$ [38,43], as most obvious from the pronounced signature peak at 27.7°. As chlorine was introduced, a clear structural transition occurred: the dimer-phase signature peak at 27.7° first decreased ($x = 1$) and then fully disappeared ($x \geq 2$). In particular, films of $Cs_3Sb_2Cl_2I_7$ and $Cs_3Sb_2Cl_3I_6$ ($x = 2, 3$ as per precursor mixing ratios) exhibited only two peaks in the region between 25° and 30° (specifically at 25.9° and 29.9°), closely matching the standard XRD pattern of layered $Cs_3Sb_2I_9$ [38]. In fact, this consistency extended to the entire pattern. This indicates that $Cs_3Sb_2Cl_2I_7$ and $Cs_3Sb_2Cl_3I_6$ films (as per precursor mixing ratios) were consistent with the layered phase. Such conversion to a layered phase was robust with respect to chlorine addition and was also reproducible, as confirmed by the absence of the dimer-phase signature peak at 27.7° in the many instances in which we characterized the XRD patterns of our $Cs_3Sb_2Cl_3I_6$ films. At higher chlorine content ($x = 4$), the same peaks appeared over the 25° – 30° range that are consistent with the layered phase. In addition to the peaks also

observed from the $x = 2, 3$ samples, other peaks also became visible (e.g., over $21° - 23°$, and at around $32.5°$ and $53.5°$), which nonetheless are consistent with the layered phase (see **Fig. S2**) and thus simply reflect a different texture in the $x = 4$ sample. In summary, while our $Cs_3Sb_2I_9$ films manifested a zero-dimensional structure, Cl incorporation enabled a robust and reproducible conversion to a two-dimensional structure for $x = 2 - 4$, with some of the iodine being replaced with chlorine.

In addition to clarifying the structural identity of our films, XRD patterns also provided insight into their orientation and morphology. The large peaks at $25.9°$ and $29.9°$ were very close in intensity (**Fig. 2**a), indicating that all our layered $Cs_3Sb_2Cl_xI_{9-x}$ films did not manifest a preferential crystalline orientation with the octahedral sheets parallel to the substrate surface. Importantly, this is in contrast to other layered cesium-antimony halides (and also other all-inorganic A-Sb-Xs) in the literature, which reports oriented films with the perovskite sheets predominantly parallel to the substrate [26,29,30]. If we consider the potential of our perovskite films within a sandwich-type device architecture, their unoriented character is expected to offer more efficient charge collection than it would be possible with an in-plane orientation.

For the purpose of evaluating how the target composition (as per precursor molar ratios) compared to the actual composition, we also analyzed our $Cs_3Sb_2Cl_xI_{9-x}$ films through Energy-Dispersive X-ray Spectroscopy (EDS). We found that those films contained less chlorine than the target amount (**Table S1**), with good uniformity across different topographical features (see **Fig. S3**). This was independent of the temperature T_{anneal} of the annealing step for $T_{anneal} \leq 150\ °C$, and consistent with Thermogravimetric Analysis (TGA)

data (**Fig. S4**). For instance, x was approximately equal to 2 in films of target composition $Cs_3Sb_2Cl_3I_6$ (as per precursor mixing ratios). Based on these indications, all additional experiments reported in the following were carried out with an annealing temperature of 135 °C. This confirms that the structural conversion revealed by XRD data was achieved through the substitution of some of the iodine with chlorine. While keeping in mind the lower-than-nominal chlorine content of our compounds, for the sake of simplicity in the following we nonetheless refer to them through their target formulas (as per precursor mixing ratios), unless the difference with the actual composition is relevant to the discussion.

The structural conversion ensuing I-to-Cl substitution had a considerable impact on the optical absorption of $Cs_3Sb_2Cl_xI_{9-x}$ films compared to the reference $Cs_3Sb_2I_9$ case. While all films delivered an in-band absorption coefficient of $> 1 \cdot 10^5$ cm^{-1}, their absorbance spectra showed a clear red shift upon Cl incorporation (**Fig. S5**). Indeed, while $Cs_3Sb_2I_9$ manifested an apparent absorption onset at a wavelength of around 500 nm, the apparent onset of other Cl-substituted films ($1 \leq x \leq 3$) was located at a wavelength of around 600 nm. In this respect, Tauc analysis (shown in **Fig. 2**b for $Cs_3Sb_2I_9$ and $Cs_3Sb_2Cl_3I_6$) was particularly revealing. (Tauc analysis of other Cl-containing compounds for $1 \leq x \leq 3$ showed significant overlap with the $Cs_3Sb_2Cl_3I_6$ case, as per **Fig. S6**.) Tauc plots firstly revealed that $Cs_3Sb_2I_9$ and $Cs_3Sb_2Cl_3I_6$ had an indirect transition at lower energy than the direct one, specifically at 1.95 eV (636 nm) for both. At the same time, while the direct transition of $Cs_3Sb_2I_9$ was at 2.37 eV (523 nm), the one of $Cs_3Sb_2Cl_3I_6$ was at 2.05 eV (605 nm). Incidentally, we note that a semiconductor with a direct gap of 2.05 eV is close to the optimal range for the top-cell in four-terminal tandem photovoltaics. For the sake of

illustration, the Shockley Queisser limit points to an ultimate power conversion efficiency (PCE) approaching 40% in combination with crystalline silicon [23,48]. In addition, such a bandgap value also offers a good match with light sources relevant to indoor photovoltaics [49], and is also compatible with photodetection in the green and blue regions of the visible range [50].

Based on the Tauc analysis, we found that the difference in apparent absorption onsets of $Cs_3Sb_2I_9$ and $Cs_3Sb_2Cl_3I_6$ related to their direct optical gaps, with the one of $Cs_3Sb_2Cl_3I_6$ being significantly smaller. In addition, while the indirect transitions occurred at lower energies than the direct ones in both compounds, the energy difference between the two transitions was particularly small for $x = 3$. Considering the higher strength of direct optical transitions, this finding implies that, to practical effects, the $x = 3$ compound behaved similarly to a direct-gap semiconductor, contrary to the case of its 0D parent compound (i.e., $Cs_3Sb_2I_9$). Finally, it is useful to compare our findings with the direct and indirect optical gaps of $Cs_3Sb_2I_9$ reported in the literature. The optical gaps of our $Cs_3Sb_2I_9$ films are consistent with the literature values of dimer-phase $Cs_3Sb_2I_9$, while the $Cs_3Sb_2Cl_3I_6$ ones conform to those of layered-phase $Cs_3Sb_2I_9$ [26,30]. This gives further evidence of the 0D-to-2D structural conversion achieved via I-to-Cl substitution, and additionally points to the electronic similarity of $Cs_3Sb_2Cl_xI_{9-x}$ with layered $Cs_3Sb_2I_9$.

Considering their relevance to optoelectronic device operation, we additionally characterized the key energy levels of the various $Cs_3Sb_2Cl_xI_{9-x}$ thin films via Ultraviolet Photoelectron Spectroscopy (UPS) (see **Fig. 2**c). As extracted from the secondary electron cutoff values, the work functions of $Cs_3Sb_2Cl_3I_6$ and $Cs_3Sb_2I_9$ amounted to 4.56 eV and

4.67 eV, respectively. In addition, from the valence band onsets we derived that the valence band maxima of $Cs_3Sb_2Cl_3I_6$ and $Cs_3Sb_2I_9$ were at 5.36 eV and 5.27 eV (respectively) below the vacuum level. Consequently, under the assumption of negligible excitonic effects, UPS and UV-Vis absorption data indicated that the conduction band minima of $Cs_3Sb_2Cl_3I_6$ and $Cs_3Sb_2I_9$ were at 3.41 eV and 3.32 eV (respectively) below the vacuum level. It is worth noting that the energy band edges extracted for $Cs_3Sb_2Cl_3I_6$ are in good agreement with the literature values of 2D $Cs_3Sb_2I_9$ [26,29], confirming once more the electronic similarity between the two layered compounds.

For the purpose of assessing their photoconversion potential, $Cs_3Sb_2Cl_xI_{9-x}$ films were embedded within a sandwich-type device stack. The structure we originally considered was as follows: glass|FTO|c-TiO$_2$|m-TiO$_2$|$Cs_3Sb_2Cl_xI_{9-x}$|poly-TPD|Au (FTO, fluorine-doped tin-oxide; c-TiO$_2$, compact titania; m-TiO$_2$, mesoporous titania; poly-TPD, poly(N,N'-bis-4-butylphenyl-N,N'-bisphenyl)benzidine) (**Fig. 3**a). The choice of the FTO|TiO$_2$ assembly as the cathode plus electron transport layer and of Au|poly-TPD as the anode plus hole transport layer was based on energetic considerations (**Fig. 3**a).

As a prototypical approach to characterizing their photoconversion potential, we evaluated the current density-voltage (J-V) characteristics of the aforementioned $Cs_3Sb_2Cl_xI_{9-x}$ devices under AM1.5G illumination (**Fig. 3**b). We emphasize that this specific characterization was considered because it allows a straightforward comparison with the prior literature on relevant compounds. In fact, based on their optical absorption properties, the photovoltaic applications most promising for $Cs_3Sb_2Cl_xI_{9-x}$ are multi-junction cells and indoor light harvesting. The key performance parameters obtained under AM1.5G

illumination are summarized in **Table 1**, while their experimental distribution is shown in **Fig. S7.** In all cases, minor hysteresis was observed (**Fig. S8**), as revealed by the calculated hysteresis index (($PCE_{Reverse}$ - $PCE_{Forward}$)/$PCE_{Reverse}$ [51]) (**Fig. 3**c). Devices based on $Cs_3Sb_2I_9$ (dimer phase) gave a PCE of 0.24%, with a short circuit current density (J_{sc}) of 1.37 mA cm^{-2}, an open-circuit voltage (V_{oc}) of 0.51 V, and a fill factor (FF) of 34% (**Fig. 3**b). In contrast, all Cl-containing photoactive layers delivered significantly higher performance (**Fig. 3**b). The maximum PCE (1.56%) was achieved with $Cs_3Sb_2Cl_3I_6$ ($x = 3$), which delivered a threefold enhancement in J_{sc} (4.94 mA cm^{-2}), an improved V_{oc} (0.70 V), and a 60% increase in FF (54%) compared to the dimer case. While the performance dramatically improved for x going from 0 to 3, in fact, a further increase in chlorine content was counterproductive, with $Cs_3Sb_2Cl_4I_5$ delivering a PCE of only 0.59% (**Table S2**). In passing, we note that the highest PCE was obtained with SVA layers (see **Fig. S9**), in line with their superior microstructure. Furthermore, we observed that the aforementioned non-encapsulated $Cs_3Sb_2Cl_3I_6$ devices exhibited good stability when stored in an N_2-filled glove box (their PCE remains at 90% of the initial value over a period of 33 days, see **Fig. S10**). Their stability in air was reduced to some extent (their PCE remains at 69% of the initial value after 33 days, see **Fig. S10**), likely resulting from the appearance of a fractional amount of phase impurities (see **Fig. S11**)—the occurrence of which, however, could be suppressed by simply coating the $Cs_3Sb_2Cl_3I_6$ layer with a 400-nm-thick PMMA film (see **Fig. S11**).

As a further optimization effort, we additionally investigated a number of alternative organic HTLs. We found that another commercial compound, LZ-HTL-1-1, could lead to higher efficiency under AM1.5G illumination. Indeed, with the same device stack

considered earlier but with poly-TPD replaced with LZ-HTL-1-1, the PCE of $Cs_3Sb_2Cl_3I_6$ devices reached up to 2.15% (**Fig. 3**b). By contrast, this resulted in lower performance with dimer-phase $Cs_3Sb_2I_9$ (**Fig. S8**). The photovoltaic performance improvement of $Cs_3Sb_2Cl_3I_6$ with this different hole transport layer was associated with a considerable boost in J_{sc} (6.46 mA cm^{-2}) and FF (55.7%), slightly offset by a V_{oc} reduction (0.6 V) (**Fig. 3**b). While LZ-HTL-1-1 possesses the same energy levels as poly-TPD (**Fig. S12**), it provides a threefold higher hole mobility (**Fig. S12**), which explains the observed performance improvement. A PCE of 2.15% constitutes nearly a 50% improvement over the highest reported efficiencies of all-inorganic layered antimony-halide perovskites in the literature (1.49%), and also nearly twice the PCE of closely-related bismuth-based homologs (1.15%) (**Table 2**) [24,26,28–31,39]. Along with their absorption onset of ≈ 600 nm, such performance figures indicate that $Cs_3Sb_2Cl_xI_{9-x}$ compounds have considerable potential for multi-junction and indoor photovoltaics [52].
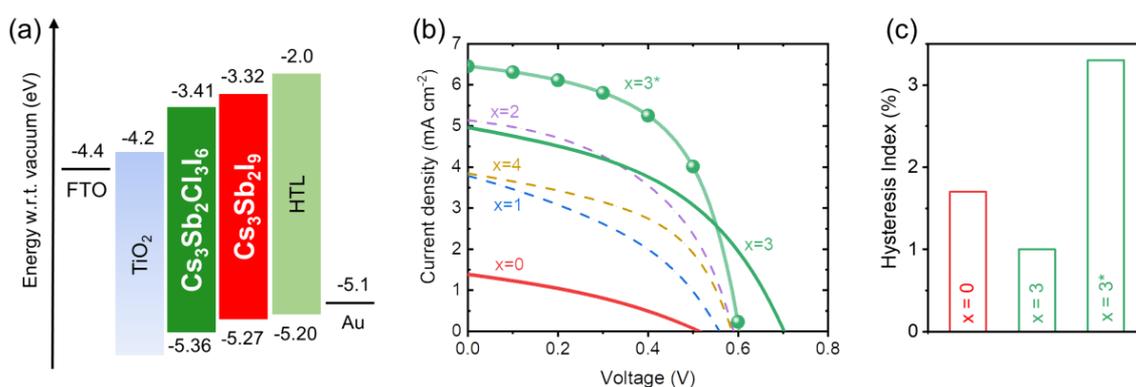

Fig. 3. $Cs_3Sb_2Cl_xI_{9-x}$ device performance under AM1.5G illumination. (a) Energy levels of representative component layers. (b) J-V characteristics. (c) Hysteresis index for $x = 0$ and $x = 3$. The $x = 3*$ device had LZ-HTL-1-1 as HTL, while all other devices had poly-TPD.

Table 1

Performance parameters (under simulated AM1.5G illumination) of as-fabricated devices based on $Cs_3Sb_2I_9$ and $Cs_3Sb_2Cl_3I_6$. Both average and best values (as per PCE) are listed. Average values and standard deviations (listed within brackets) were calculated from 12 devices of each type.

	V_{oc} (V)	J_{sc} (mA cm^{-2})	FF (%)	PCE (%)
$x = 0$	0.51 (0.50 ± 0.01)	1.37 (1.33 ± 0.08)	34 (35 ± 1.17)	0.24 (0.22 ± 0.02)
$x = 3$[a)]	0.60 (0.61 ± 0.05)	6.46 (5.77±0.47)	56 (50 ± 2.93)	2.15 (1.76± 0.15)

[a)] With LZ-HTL-1-1 as HTL.

Table 2

Photovoltaic performance parameters from the literature on all-inorganic 2D antimony-/bismuth-halide perovskites (i.e., $A_3M_2X_9$, A$^+$: inorganic cation, M: Sb^{3+}/Bi^{3+}, X$^-$: halide anion(s)). If available, average and standard deviation values are reported within brackets, while all other values are from champion or representative devices.

Ref.	Active Layer	V_{oc} [V]	J_{sc} [mA cm^{-2}]	FF [%]	PCE [%]	EQE_{max} [%]
[26]	$Cs_3Sb_2I_9$	≈ 0.30	≈ 0.05	≈ 34	≈ 0.005	-
[29]	$Cs_3Sb_2I_9$	0.72 (0.68±0.04)	5.31 (4.62±0.71)	38.97 (37.14±2.75)	1.49 (1.26±0.18)	40
[30]	$Cs_3Sb_2I_9$	0.61	3.55	55.85	1.21	32
[28]	$Rb_3Sb_2I_9$	0.55 (0.52±0.02)	2.11 (1.66±0.28)	56.97 (56.56±2.29)	0.66 (0.66±0.09)	32.8
[31]	$Rb_3Sb_2Br_{9-x}I_x$	0.55 (0.51±0.03)	4.25 (3.80±0.44)	59.56 (55.1±3.8)	1.37 (1.06±0.12)	26.7
[24]	$Rb_3Sb_2I_9$	0.66	1.84	63	0.76	-
[24]	$K_3Sb_2I_9$	0.34	0.41	50	0.07	-
[39]	$Cs_3Bi_2Br_xI_{9-x}$	0.64	3.15	57	1.15	32

Insight into the impact of I-to-Cl substitution on the photoconversion process could be gained by considering the external quantum efficiency (EQE) of $Cs_3Sb_2Cl_3I_6$ (2D) and $Cs_3Sb_2I_9$ (0D) devices (**Fig. 4**a). The EQE spectra of both devices matched well with the absorption spectra of their photoactive layers. Indeed, $Cs_3Sb_2I_9$ (0D) devices manifested an EQE onset slightly below 550 nm, while the same was at around 600 nm for $Cs_3Sb_2Cl_3I_6$ (2D) devices (compare with the direct optical gaps of the two materials shown in **Fig. 2**b).

In addition, the corresponding integrated photocurrents (**Fig. 4**a) closely matched the photovoltaic measurements (**Fig. 3**b). Most importantly, the peak EQE of $Cs_3Sb_2I_9$ (0D) devices was at 30.7%, while $Cs_3Sb_2Cl_3I_6$ (2D) devices gave 62.5%. This highlights the substantial improvement in photoconversion efficiency enabled by the 0D-to-2D conversion. It is worth noting that an EQE of 62.5% marks a considerable improvement over all the prior literature on layered inorganic antimony-halide perovskites (**Table 2**) [24,26,28–31]. In fact, a peak EQE of 62.5% is at the state of the art for all antimony-/bismuth-halide perovskites (i.e., compounds with formula $A_3M_2X_9$, where A^+ is an organic/inorganic cation, M^{3+} is Sb^{3+}/Bi^{3+}, and X^- is a halide anion) (**Table S3**).

Photocurrent measurements at variable optical power enable insight into the photoconversion mechanism, as they probe the (sub-bandgap) energetic landscape swept by the quasi-Fermi levels [53–55] and/or effects arising from space-charge build up within the photoactive layer [56]. Therefore, we experimentally assessed the photocurrent-optical power characteristics of $Cs_3Sb_2Cl_3I_6$ (2D) and $Cs_3Sb_2I_9$ (0D) devices over an optical power range of $\approx$ 1–100 mW cm^{-2}. We did so by illuminating the devices with light pulses of wavelength λ = 505 nm while the devices were kept in short circuit conditions. Pulsed illumination was adopted in order to avoid heating effects and also as a further probe into the photoconversion process. We found that both 0D and 2D compounds delivered photocurrent transients exhibiting a monotonic rise to their steady state (**Fig. S13**). Therefore, it is possible to rule out the occurrence of a space-charge build-up (due to trapped [56] or free carriers [57]) in the photoactive layers. The steady-state photocurrent values at variable power ($I_{ph} - P_{opt}$ characteristics) are plotted on a double-logarithmic
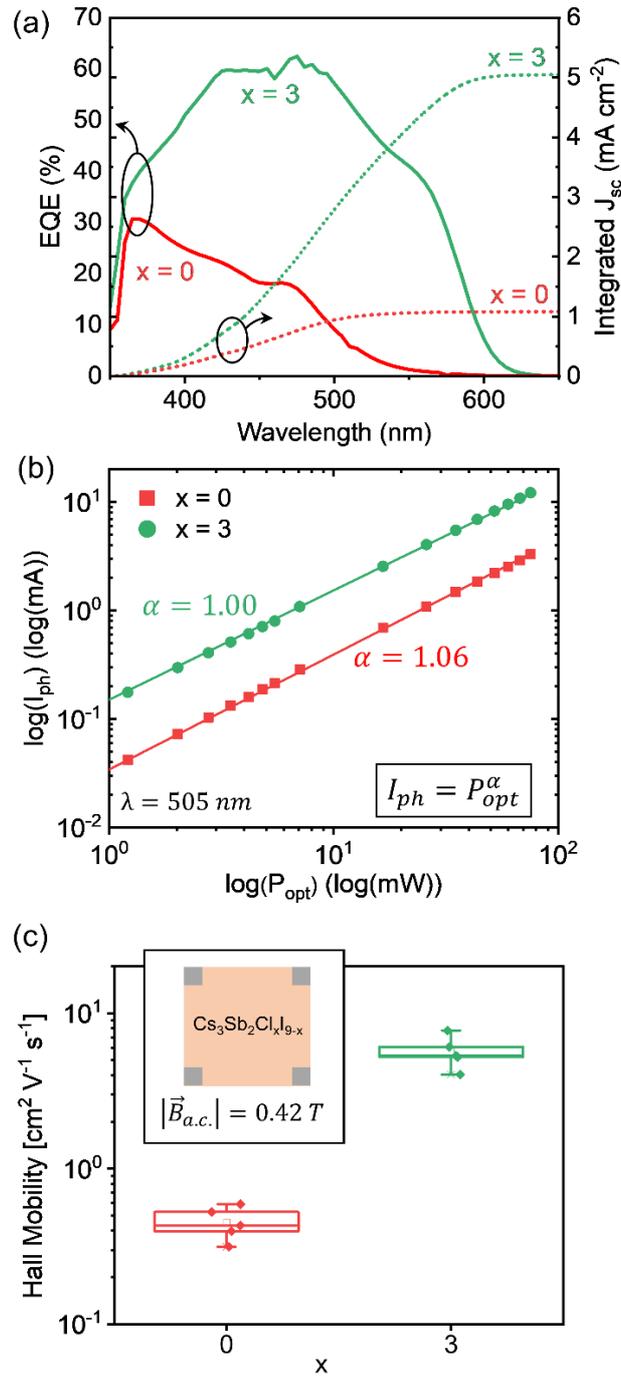
Fig. 4. (a) External quantum efficiency of $Cs_3Sb_2Cl_3I_6$ (2D) and $Cs_3Sb_2I_9$ (0D) devices (at 0 V applied bias). (b) Photocurrent-optical power characteristics of $Cs_3Sb_2Cl_3I_6$ (2D) and $Cs_3Sb_2I_9$ (0D) devices (at 0 V applied bias). (c) Hall mobility of $Cs_3Sb_2Cl_3I_6$ (2D) and $Cs_3Sb_2I_9$ (0D) films (inset: Hall sample structure).

22

scale in **Fig. 4**b. Datasets from both $Cs_3Sb_2Cl_3I_6$ (2D) and $Cs_3Sb_2I_9$ (0D) devices conform to a straight-line fit with slope indistinguishable from unity, implying that they both follow a dependence of the type $I_{ph} \propto P_{opt}^\gamma$ with $\gamma = 1$. In reference to the one- and two-center recombination models of the Rose-Bube theory [53–55,58], having $\gamma = 1$ allows us to rule out band-to-band recombination as the photoconversion-limiting mechanism. Therefore, we conclude that the photocurrent in both $Cs_3Sb_2Cl_3I_6$ (2D) and $Cs_3Sb_2I_9$ (0D) was limited by one-center recombination (i.e., recombination through one type of deep levels).

We additionally assessed the charge transport properties of both $Cs_3Sb_2Cl_3I_6$ (2D) and $Cs_3Sb_2I_9$ (0D) in order to clarify the observed photoconversion behavior. We thus conducted Hall effect characterization with modulated magnetic field on thin-films of $Cs_3Sb_2Cl_3I_6$ (2D) and $Cs_3Sb_2I_9$ (0D) (processed according to the same deposition procedure adopted for device fabrication). In particular, these films were embedded within van der Pauw devices (see the inset of **Fig. 4**c and Section 2.7 for details). We note that conventional constant-magnetic-field Hall characterization on high-resistivity perovskites is generally challenging, since it is limited by artifacts due to geometric non-idealities and thermo-galvanomagnetic effects. Therefore, in order to overcome this limitation, we resorted to AC-magnetic-field Hall effect characterization. This choice was motivated by the fact that a modulated (i.e., AC) magnetic field allows the measured Hall voltage (detected via a lock-in amplifier) to be desensitized from the aforementioned artifacts [59]. Indeed, the AC-magnetic-field methodology has been demonstrated to allow the reliable characterization of the Hall effect in materials with mobilities reaching down to well below $1 \text{ cm}^2 \text{ V}^{-1} \text{ s}^{-1}$ [59–62]. In our Hall experiments, we specifically applied an AC magnetic field with root-mean-square amplitude of 0.42291 T and modulation frequency of 100

mHz. These measurements were conducted at variable excitation current, from which near-constant Hall mobility values were obtained, consistently with basic Hall effect phenomenology (**Fig. S14**). In particular, we found that the average Hall mobility of our $Cs_3Sb_2Cl_3I_6$ (2D) films was 5.7 $cm^2\,V^{-1}\,s^{-1}$, while $Cs_3Sb_2I_9$ (0D) films gave a Hall mobility of 0.5 $cm^2\,V^{-1}\,s^{-1}$ (**Fig. 4**c and **Table S4**). Due to the unoriented character of our films (as per XRD), these Hall mobility values measured in the in-plane direction would be representative of the charge carrier transport in the out-of-plane direction that is relevant to our device operation. The association of a higher photoconversion efficiency with a dramatic improvement in charge carrier mobility points to the following working mechanism of our $Cs_3Sb_2Cl_xI_{9-x}$ devices under illumination: a) some of the mobile carriers photogenerated in the active layer (i.e., $Cs_3Sb_2Cl_xI_{9-x}$) may undergo non-geminate recombination prior to being collected at the electrodes; b) a higher carrier mobility ensures a faster transit time of the photocarriers to the electrodes, hence it allows a higher fraction of photocarriers to escape recombination and contribute to the photocurrent [63] (for instance, leading to a higher EQE). We therefore attribute the observed improvement in photoconversion and photovoltaic efficiencies to the significantly higher mobility of $Cs_3Sb_2Cl_3I_6$ compared to the 0D counterpart.

Apart from clarifying our photoconversion data, our charge transport characterization offers insight in regard to the capabilities and potential of 2D antimony-halide perovskites and related materials (e.g., bismuth-based). In this respect, it is firstly useful to refer to the computational studies on $Cs_3Sb_2I_9$ by Correa-Baena et al. and Saparov et al. [24,26]. These studies highlighted the transport anisotropy of the 2D phase of $Cs_3Sb_2I_9$ (with superior transport being achieved within the octahedral sheets) and also jointly showed that the 0D

phase features much larger carrier effective masses. In addition to their general agreement with our transport experiments, these computational findings enable us to put in context the substantial boost in photoconversion efficiency achieved with our layered $Cs_3Sb_2Cl_3I_6$ films. Indeed, our layered films possess an unoriented character, thus our devices could benefit to a good extent from the facile charge transport within the octahedral sheets. In contrast, all photovoltaic studies on layered $Cs_3Sb_2I_9$ to date relied on oriented films with the octahedral sheets predominantly parallel to the substrate [26,29,30]. In fact, this was also the case for other layered all-inorganic antimony-halide-perovskite studies [24,28,31]. Consequently, considering the electronic similarity between 2D $Cs_3Sb_2I_9$ and $Cs_3Sb_2Cl_3I_6$, the photoconversion efficiency enhancement attained with our layered films can be related to their unoriented character, which provides them with a charge transport edge. It is also interesting that closely-related $Cs_3Bi_2Br_xI_{9-x}$, a 2D all-inorganic bismuth-halide homolog, delivered an EQE of 32% (approximately half the EQE of $Cs_3Sb_2Cl_3I_6$) while relying on oriented films with in-plane perovskite sheets [39]. All this indicates that layered all-inorganic antimony halides (and their bismuth-halide homologs) could potentially deliver higher photovoltaic performance by aligning their perovskite sheets in the out-of-plane direction, in fact, as seen in layered lead-based-perovskite studies [32,33].

4. Conclusion

This work established a solution-based low-temperature (100 – 150 °C) route to the conversion of zero-dimensional $Cs_3Sb_2I_9$ into a layered structure. This was achieved by the substitution of some of the iodine with chlorine and was accompanied by a reduction of the direct optical gap to 2.05 eV. This approach thus provided a route to the structural conversion of the cesium-antimony-halide system alternative to the high-temperature (≥

230 °C) treatments reported in the prior literature on the cesium-antimony-halide system. In addition, we found that our synthetic approach resulted in layered films that do not exhibit preferential orientation of the octahedral planes. This is in contrast to the high-temperature-processed cesium-antimony halides from the literature, which showed preferential out-of-plane orientation (non-ideal for charge transport within a sandwich-type device structure).

To assess the optoelectronic significance of our structural conversion route, we evaluated the photoconversion properties of devices comprising our layered compounds. The attained EQE was up to 62.5%, marking a considerable improvement over all the prior literature on layered all-inorganic antimony-halide perovskites [24,26,28–31,39]. In addition, under AM1.5G illumination, $Cs_3Sb_2Cl_3I_6$ devices delivered a PCE setting the new state of the art for two-dimensional all-inorganic antimony-halide perovskites and bismuth-based homologs [24,26,28–31,39].

Detailed optoelectronic characterization was carried out to identify the origin of the observed photoconversion efficiency improvement. Through Hall effect characterization, we found a dramatic charge transport improvement, leading to a Hall mobility value of 5.7 cm^2 V^{-1} s^{-1} in two-dimensional $Cs_3Sb_2Cl_3I_6$. We were thus able to reveal the close relationship between the observed photoconversion efficiency boost and the improvement in charge transport properties, which enabled a larger fraction of photocarriers to reach the collecting electrodes, in accordance with general photoconversion models that apply to perovskites and derivatives [63,64].

The attained device performance levels point to the considerable potential of our all-inorganic layered compounds for multi-junction photovoltaics, indoor photovoltaics, and photodetection. Indeed, in a tandem configuration with crystalline silicon, an efficient photoactive material with bandgap in the region of 2.0 eV—as our 2D $Cs_3Sb_2Cl_3I_6$—could ultimately lead to a power conversion of ~ 40% under solar illumination [23,48]. Additionally, considering the large photoconversion efficiency of $Cs_3Sb_2Cl_3I_6$ as well as the excellent match of its bandgap with the emission of indoor light sources [49], it can be envisaged that $Cs_3Sb_2Cl_3I_6$ could offer an appealing solution for high-efficiency indoor photovoltaics. Lastly, the highly efficient photoconversion of $Cs_3Sb_2Cl_3I_6$ in the blue and green regions paves the way for its exploration for solution-processed low-cost photodetectors aiming to address emerging application domains such as the Internet of things, computer vision, and visible light communications [65].

On the basis of our findings, valuable indications can be extrapolated on future directions that could deliver further improvements in the photoconversion efficiency of 2D $Cs_3Sb_2Cl_3I_6$. Firstly, considering the role of microstructure in determining charge transport and photoconversion efficiency, it can be anticipated that further efforts aiming to improve the grain size of solution-deposited $Cs_3Sb_2Cl_3I_6$ films could further boost their EQE. Additionally, considering the random orientation of the octahedral sheets in our films and the correlation of charge transport and photoconversion efficiency, it can be envisaged that higher photoconversion efficiency could be achieved in sandwich-type devices by developing strategies for the preferential out-of-plane alignment of the octahedral sheets. In fact, our findings suggest that this a general priority for layered all-inorganic antimony-/bismuth-halide perovskites. Lastly, at a device level, it can be expected that further

optimization of other functional layers or materials used in $Cs_3Sb_2Cl_3I_6$ devices could also deliver a photoconversion efficiency boost—e.g., doping of TiO_2 [66], use of alternative nanostructured transport layers [67,68], and incorporation of up- and down-conversion materials [69,70].

The low-temperature route to the structural conversion of $Cs_3Sb_2I_9$, the ensuing enhancement in photoconversion efficiency, and the resulting insight into the current and perspective capabilities of all-inorganic antimony-halide perovskites constitute an important step in realizing the full potential of these all-inorganic compounds for lead-free optoelectronic applications.

Data availability

The data that support the findings of this study are available from the corresponding author upon reasonable request.

Declaration of Competing Interest

L. F. is founder and CEO of Wuhan LinkZill Technology Co., Ltd.

Acknowledgments

Funding Sources

Appendix A. Supplementary data

Supplementary material related to this article can be found, in the online version at doi: TBD.

References

[1]   M. Kim, G.-H. Kim, T.K. Lee, I.W. Choi, H.W. Choi, Y. Jo, Y.J. Yoon, J.W. Kim, J. Lee, D. Huh, H. Lee, S.K. Kwak, J.Y. Kim, D.S. Kim, Methylammonium Chloride Induces Intermediate Phase Stabilization for Efficient Perovskite Solar Cells, Joule. 3 (2019) 2179–2192. https://doi.org/10.1016/j.joule.2019.06.014.

[2]   X. Zheng, J. Troughton, N. Gasparini, Y. Lin, M. Wei, Y. Hou, J. Liu, K. Song, Z. Chen, C. Yang, B. Turedi, A.Y. Alsalloum, J. Pan, J. Chen, A.A. Zhumekenov, T.D. Anthopoulos, Y. Han, D. Baran, O.F. Mohammed, E.H. Sargent, O.M. Bakr, Quantum Dots Supply Bulk- and Surface-Passivation Agents for Efficient and Stable Perovskite Solar Cells, Joule. 3 (2019) 1963–1976. https://doi.org/10.1016/j.joule.2019.05.005.

[3]   P.K. Nayak, S. Mahesh, H.J. Snaith, D. Cahen, Photovoltaic solar cell technologies: analysing the state of the art, Nat. Rev. Mater. 4 (2019) 269–285. https://doi.org/10.1038/s41578-019-0097-0.

[4]   A.K. Jena, A. Kulkarni, T. Miyasaka, Halide Perovskite Photovoltaics: Background, Status, and Future Prospects, Chem. Rev. 119 (2019) 3036–3103. https://doi.org/10.1021/acs.chemrev.8b00539.

[5]   M.D. Smith, B.A. Connor, H.I. Karunadasa, Tuning the Luminescence of Layered Halide Perovskites, Chem. Rev. 119 (2019) 3104–3139. https://doi.org/10.1021/acs.chemrev.8b00477.

[6]   J. Zhou, J. Huang, Photodetectors Based on Organic–Inorganic Hybrid Lead Halide Perovskites, Adv. Sci. 5 (2018) 1700256. https://doi.org/10.1002/advs.201700256.

[7]   M.-C. Tang, Y. Fan, D. Barrit, X. Chang, H.X. Dang, R. Li, K. Wang, D.-M. Smilgies, S. (Frank) Liu, S. De Wolf, T.D. Anthopoulos, K. Zhao, A. Amassian, Ambient blade coating of mixed cation, mixed halide perovskites without dripping: in situ investigation and highly efficient solar cells, J. Mater. Chem. A. 8 (2020) 1095–1104. https://doi.org/10.1039/C9TA12890E.

[8]   K. Wang, M.-C. Tang, H.X. Dang, R. Munir, D. Barrit, M. De Bastiani, E. Aydin, D.-M. Smilgies, S. De Wolf, A. Amassian, Kinetic Stabilization of the Sol-Gel State in Perovskites Enables Facile Processing of High-Efficiency Solar Cells, Adv. Mater. 31 (2019) 1808357. https://doi.org/10.1002/adma.201808357.

[9]   D. Barrit, P. Cheng, M. Tang, K. Wang, H. Dang, D. Smilgies, S. (Frank) Liu, T.D. Anthopoulos, K. Zhao, A. Amassian, Impact of the Solvation State of Lead Iodide on Its Two-Step Conversion to MAPbI 3 : An In Situ Investigation, Adv. Funct. Mater. 29 (2019) 1807544. https://doi.org/10.1002/adfm.201807544.

[10]   D. Barrit, P. Cheng, K. Darabi, M. Tang, D. Smilgies, S. (Frank) Liu, T.D. Anthopoulos, K. Zhao, A. Amassian, Room-Temperature Partial Conversion of α-FAPbI 3 Perovskite Phase via PbI 2 Solvation Enables High-Performance Solar Cells, Adv. Funct. Mater. 30 (2020) 1907442. https://doi.org/10.1002/adfm.201907442.

[11]   NREL, N.R.E.L. Research Cell Record Efficiency Chart, (2019). https://www.nrel.gov/pv/cell-efficiency.html (accessed September 25, 2019).

[12]   A. Babayigit, A. Ethirajan, M. Muller, B. Conings, Toxicity of organometal halide perovskite solar cells, Nat. Mater. 15 (2016) 247–251. https://doi.org/10.1038/nmat4572.

[13]   V. Pecunia, Y. Yuan, J. Zhao, K. Xia, Y. Wang, S. Duhm, L. Portilla, F. Li, Perovskite-Inspired Lead-Free Ag2BiI5 for Self-Powered NIR-Blind Visible Light Photodetection, Nano-Micro Lett. 12 (2020) 27. https://doi.org/10.1007/s40820-020-0371-0.

[14]   R. Wang, J. Wang, S. Tan, Y. Duan, Z.-K. Wang, Y. Yang, Opportunities and Challenges of Lead-Free Perovskite Optoelectronic Devices, Trends Chem. 1 (2019) 368–379. https://doi.org/10.1016/j.trechm.2019.04.004.

[15]   Q. Zhang, H. Ting, S. Wei, D. Huang, C. Wu, W. Sun, B. Qu, S. Wang, Z. Chen, L. Xiao, Recent progress in lead-free perovskite (-like) solar cells, Mater. Today Energy. 8 (2018) 157–165.

https://doi.org/10.1016/j.mtener.2018.03.001.

[16] A. Abate, Perovskite Solar Cells Go Lead Free, Joule. 1 (2017) 659–664. https://doi.org/10.1016/j.joule.2017.09.007.

[17] L.C. Lee, T.N. Huq, J.L. MacManus-Driscoll, R.L.Z. Hoye, Research Update: Bismuth-based perovskite-inspired photovoltaic materials, APL Mater. 6 (2018) 084502. https://doi.org/10.1063/1.5029484.

[18] M.-C. Tang, D. Barrit, R. Munir, R. Li, J.M. Barbé, D.-M. Smilgies, S. Del Gobbo, T.D. Anthopoulos, A. Amassian, Bismuth-Based Perovskite-Inspired Solar Cells: In Situ Diagnostics Reveal Similarities and Differences in the Film Formation of Bismuth- and Lead-Based Films, Sol. RRL. 3 (2019) 1800305. https://doi.org/10.1002/solr.201800305.

[19] S.M. Jain, T. Edvinsson, J.R. Durrant, Green fabrication of stable lead-free bismuth based perovskite solar cells using a non-toxic solvent, Commun. Chem. 2 (2019) 91. https://doi.org/10.1038/s42004-019-0195-3.

[20] Z. Xiao, Z. Song, Y. Yan, From Lead Halide Perovskites to Lead-Free Metal Halide Perovskites and Perovskite Derivatives, Adv. Mater. (2019) 1803792. https://doi.org/10.1002/adma.201803792.

[21] A.M. Ganose, C.N. Savory, D.O. Scanlon, Beyond methylammonium lead iodide: prospects for the emergent field of ns 2 containing solar absorbers, Chem. Commun. 103 (2016) 15729–15735. https://doi.org/10.1039/C6CC06475B.

[22] R.L.Z. Hoye, R.E. Brandt, A. Osherov, V. Stevanović, S.D. Stranks, M.W.B. Wilson, H. Kim, A.J. Akey, J.D. Perkins, R.C. Kurchin, J.R. Poindexter, E.N. Wang, M.G. Bawendi, V. Bulović, T. Buonassisi, Methylammonium Bismuth Iodide as a Lead-Free, Stable Hybrid Organic-Inorganic Solar Absorber, Chem. - A Eur. J. 22 (2016) 2605–2610. https://doi.org/10.1002/chem.201505055.

[23] J.-C. Hebig, I. Kühn, J. Flohre, T. Kirchartz, Optoelectronic Properties of (CH3NH3)3Sb2I9 Thin Films for Photovoltaic Applications, ACS Energy Lett. 1 (2016) 309–314. https://doi.org/10.1021/acsenergylett.6b00170.

[24] J.-P. Correa-Baena, L. Nienhaus, R.C. Kurchin, S.S. Shin, S. Wieghold, N.T. Putri Hartono, M. Layurova, N.D. Klein, J.R. Poindexter, A. Polizzotti, S. Sun, M.G. Bawendi, T. Buonassisi, A-Site Cation in Inorganic A3Sb2I9 Perovskite Influences Structural Dimensionality, Exciton Binding Energy, and Solar Cell Performance, Chem. Mater. 30 (2018) 3734–3742. https://doi.org/10.1021/acs.chemmater.8b00676.

[25] M. Lyu, J.H. Yun, M. Cai, Y. Jiao, P. V. Bernhardt, M. Zhang, Q. Wang, A. Du, H. Wang, G. Liu, L. Wang, Organic-inorganic bismuth (III)-based material: A lead-free, air-stable and solution-processable light-absorber beyond organolead perovskites, Nano Res. 9 (2016) 692–702. https://doi.org/10.1007/s12274-015-0948-y.

[26] B. Saparov, F. Hong, J.-P. Sun, H.-S. Duan, W. Meng, S. Cameron, I.G. Hill, Y. Yan, D.B. Mitzi, Thin-Film Preparation and Characterization of Cs3Sb2I9: A Lead-Free Layered Perovskite Semiconductor, Chem. Mater. 27 (2015) 5622–5632. https://doi.org/10.1021/acs.chemmater.5b01989.

[27] A.J. Lehner, D.H. Fabini, H.A. Evans, C.A. Hébert, S.R. Smock, J. Hu, H. Wang, J.W. Zwanziger, M.L. Chabinyc, R. Seshadri, Crystal and Electronic Structures of Complex Bismuth Iodides A3Bi2I9 (A = K, Rb, Cs) Related to Perovskite: Aiding the Rational Design of Photovoltaics, Chem. Mater. 27 (2015) 7137–7148. https://doi.org/10.1021/acs.chemmater.5b03147.

[28] P.C. Harikesh, H.K. Mulmudi, B. Ghosh, T.W. Goh, Y.T. Teng, S. Mhaisalkar, N. Mathews, 8, (2016). https://doi.org/10.1021/acs.chemmater.6b03310.

[29] A. Singh, K.M. Boopathi, A. Mohapatra, Y.F. Chen, G. Li, C.W. Chu, 6, ACS Appl. Mater. Interfaces. 10 (2018) 2566–2573. https://doi.org/10.1021/acsami.7b16349.

[30] F. Umar, J. Zhang, Z. Jin, I. Muhammad, X. Yang, H. Deng, K. Jahangeer, Q. Hu, H. Song, J. Tang, Dimensionality Controlling of Cs3Sb2I9 for Efficient All-Inorganic Planar Thin Film Solar Cells by HCl-Assisted Solution Method, Adv. Opt. Mater. 7 (2019) 1801368. https://doi.org/10.1002/adom.201801368.

[31] S. Weber, T. Rath, K. Fellner, R.C. Fischer, R. Resel, B. Kunert, T. Dimopoulos, A. Steinegger, G. Trimmel, 10, (2018). https://doi.org/10.1021/acsaem.8b01572.

[32] H. Tsai, W. Nie, J.-C. Blancon, C.C. Stoumpos, R. Asadpour, B. Harutyunyan, A.J. Neukirch, R. Verduzco, J.J. Crochet, S. Tretiak, L. Pedesseau, J. Even, M.A. Alam, G. Gupta, J. Lou, P.M. Ajayan, M.J. Bedzyk, M.G. Kanatzidis, A.D. Mohite, High-efficiency two-dimensional

Ruddlesden–Popper perovskite solar cells, Nature. 536 (2016) 312–316.
https://doi.org/10.1038/nature18306.

[33]   G. Wu, X. Li, J. Zhou, J. Zhang, X. Zhang, X. Leng, P. Wang, M. Chen, D. Zhang, K. Zhao, S.
(Frank) Liu, H. Zhou, Y. Zhang, Fine Multi-Phase Alignments in 2D Perovskite Solar Cells with
Efficiency over 17% via Slow Post-Annealing, Adv. Mater. (2019) 1903889.
https://doi.org/10.1002/adma.201903889.

[34]   Y. Zhang, P. Wang, M.-C. Tang, D. Barrit, W. Ke, J. Liu, T. Luo, Y. Liu, T. Niu, D.-M. Smilgies,
Z. Yang, Z. Liu, S. Jin, M.G. Kanatzidis, A. Amassian, S.F. Liu, K. Zhao, Dynamical
Transformation of Two-Dimensional Perovskites with Alternating Cations in the Interlayer Space
for High-Performance Photovoltaics, J. Am. Chem. Soc. 141 (2019) 2684–2694.
https://doi.org/10.1021/jacs.8b13104.

[35]   R. Arai, M. Yoshizawa-Fujita, Y. Takeoka, M. Rikukawa, Factors determining the vertical
orientation of two-dimensional perovskites, CrystEngComm. 21 (2019) 4529–4533.
https://doi.org/10.1039/C9CE00631A.

[36]   Y. Liu, J. Zhang, H. Wu, W. Cui, R. Wang, K. Ding, S.-T. Lee, B. Sun, Low-temperature synthesis
TiOx passivation layer for organic-silicon heterojunction solar cell with a high open-circuit voltage,
Nano Energy. 34 (2017) 257–263. https://doi.org/10.1016/j.nanoen.2017.02.024.

[37]   V. Pecunia, M. Nikolka, A. Sou, I. Nasrallah, A.Y. Amin, I. McCulloch, H. Sirringhaus, Trap
Healing for High-Performance Low-Voltage Polymer Transistors and Solution-Based Analog
Amplifiers on Foil, Adv. Mater. 29 (2017) 1606938. https://doi.org/10.1002/adma.201606938.

[38]   K. Yamada, H. Sera, S. Sawada, H. Tada, T. Okuda, H. Tanaka, Reconstructive Phase
Transformation and Kinetics of Cs3Sb2I9 by Means of Rietveld Analysis of X-Ray Diffraction and
127I NQR, J. Solid State Chem. 134 (1997) 319–325. https://doi.org/10.1006/jssc.1997.7562.

[39]   B.-B. Yu, M. Liao, J. Yang, W. Chen, Y. Zhu, X. Zhang, T. Duan, W. Yao, S.-H. Wei, Z. He,
Alloy-induced phase transition and enhanced photovoltaic performance: the case of Cs3Bi2I9−xBr
x perovskite solar cells, J. Mater. Chem. A. 7 (2019) 8818–8825.
https://doi.org/10.1039/C9TA01978B.

[40]   K.M. McCall, C.C. Stoumpos, O.Y. Kontsevoi, G.C.B. Alexander, B.W. Wessels, M.G. Kanatzidis,
From 0D Cs3Bi2I9 to 2D Cs3Bi2I6Cl3: Dimensional Expansion Induces a Direct Band Gap but
Enhances Electron–Phonon Coupling, Chem. Mater. 31 (2019) 2644–2650.
https://doi.org/10.1021/acs.chemmater.9b00636.

[41]   T.L. Hodgkins, C.N. Savory, K.K. Bass, B.L. Seckman, D.O. Scanlon, P.I. Djurovich, M.E.
Thompson, B.C. Melot, Anionic order and band gap engineering in vacancy ordered triple
perovskites, Chem. Commun. 55 (2019) 3164–3167. https://doi.org/10.1039/C8CC09947B.

[42]   F. Jiang, D. Yang, Y. Jiang, T. Liu, X. Zhao, Y. Ming, B. Luo, F. Qin, J. Fan, H. Han, L. Zhang, Y.
Zhou, Chlorine-Incorporation-Induced Formation of the Layered Phase for Antimony-Based Lead-
Free Perovskite Solar Cells, J. Am. Chem. Soc. 140 (2018) 1019–1027.
https://doi.org/10.1021/jacs.7b10739.

[43]   B. Chabot, E. Parthé, Cs 3 Sb 2 I 9 and Cs 3 Bi 2 I 9 with the hexagonal Cs 3 Cr 2 Cl 9 structure
type, Acta Crystallogr. Sect. B Struct. Crystallogr. Cryst. Chem. 34 (1978) 645–648.
https://doi.org/10.1107/S0567740878003684.

[44]   A.E. Nielsen, Kinetics of precipitation, Pergamon Press, Oxford, UK, 1964.

[45]   W.K. Burton, N. Cabrera, F.C. Frank, The growth of crystals and the equilibrium structure of their
surfaces, Philos. Trans. R. Soc. London. Ser. A, Math. Phys. Sci. 243 (1951) 299–358.
https://doi.org/10.1098/rsta.1951.0006.

[46]   L. Reimer, Scanning Electron Microscopy, Springer Berlin Heidelberg, Berlin, Heidelberg, 1998.
https://doi.org/10.1007/978-3-540-38967-5.

[47]   J.I. Goldstein, D.E. Newbury, J.R. Michael, N.W.M. Ritchie, J.H.J. Scott, D.C. Joy, Scanning
Electron Microscopy and X-Ray Microanalysis, Springer New York, New York, NY, 2018.
https://doi.org/10.1007/978-1-4939-6676-9.

[48]   W. Shockley, H.J. Queisser, Detailed Balance Limit of Efficiency of p-n Junction Solar Cells, J.
Appl. Phys. 32 (1961) 510–519. https://doi.org/10.1063/1.1736034.

[49]   I. Mathews, S.N. Kantareddy, T. Buonassisi, I.M. Peters, Technology and market perspective for
indoor photovoltaic cells, Joule. (2019).

[50]   V. Pecunia, Efficiency and spectral performance of narrowband organic and perovskite

photodetectors: a cross-sectional review, J. Phys. Mater. 2 (2019) 042001. https://doi.org/10.1088/2515-7639/ab336a.

[51]   M.M. Tavakoli, W. Tress, J. V. Milić, D. Kubicki, L. Emsley, M. Grätzel, Addition of adamantylammonium iodide to hole transport layers enables highly efficient and electroluminescent perovskite solar cells, Energy Environ. Sci. 11 (2018) 3310–3320. https://doi.org/10.1039/C8EE02404A.

[52]   T.C. Yang, P. Fiala, Q. Jeangros, C. Ballif, High-Bandgap Perovskite Materials for Multijunction Solar Cells, Joule. 2 (2018) 1421–1436. https://doi.org/10.1016/j.joule.2018.05.008.

[53]   A. Rose, Recombination Processes in Insulators and Semiconductors, Phys. Rev. 97 (1955) 1727–1727. https://doi.org/10.1103/PhysRev.97.1727.2.

[54]   R.H. Bube, A new mechanism for superlinear photoconductivity with relevance to amorphous silicon, J. Appl. Phys. 74 (1993) 5138–5143. https://doi.org/10.1063/1.355310.

[55]   A. Rose, Performance of Photoconductors, Proc. IRE. 43 (1955) 1850–1869. https://doi.org/10.1109/JRPROC.1955.278047.

[56]   A.M. Goodman, A. Rose, Double extraction of uniformly generated electron-hole pairs from insulators with noninjecting contacts, J. Appl. Phys. 42 (1971) 2823–2830. https://doi.org/10.1063/1.1660633.

[57]   R.S. Crandall, Field nonuniformity due to photogenerated carriers in a p-i-n solar cell, RCA Rev. 42 (1981) 458–462.

[58]   R.H. Bube, Photoelectronic properties of semiconductors, Cambridge University Press, Cambridge, UK, 1992.

[59]   J. Lindemuth, S.-I. Mizuta, Hall measurements on low-mobility materials and high resistivity materials, in: Proc. SPIE 8110, Thin Film Sol. Technol. III, SPIE, 2011: p. 81100I. https://doi.org/10.1117/12.893100.

[60]   D.T. Scholes, P.Y. Yee, J.R. Lindemuth, H. Kang, J. Onorato, R. Ghosh, C.K. Luscombe, F.C. Spano, S.H. Tolbert, B.J. Schwartz, The Effects of Crystallinity on Charge Transport and the Structure of Sequentially Processed F 4 TCNQ-Doped Conjugated Polymer Films, Adv. Funct. Mater. 27 (2017) 1702654. https://doi.org/10.1002/adfm.201702654.

[61]   A.J.E. Rettie, H.C. Lee, L.G. Marshall, J.-F. Lin, C. Capan, J. Lindemuth, J.S. McCloy, J. Zhou, A.J. Bard, C.B. Mullins, Combined Charge Carrier Transport and Photoelectrochemical Characterization of BiVO 4 Single Crystals: Intrinsic Behavior of a Complex Metal Oxide, J. Am. Chem. Soc. 135 (2013) 11389–11396. https://doi.org/10.1021/ja405550k.

[62]   T. Umehara, S. Iinuma, A. Sadono, Y. Kurokawa, A. Yamada, Electrical characterization of Cu(In,Ga)Se 2 thin films peeled off from Mo-coated soda-lime glass substrate by AC Hall measurement, Jpn. J. Appl. Phys. 54 (2015) 018001. https://doi.org/10.7567/JJAP.54.018001.

[63]   H. Azimi, T. Ameri, H. Zhang, Y. Hou, C.O.R. Quiroz, J. Min, M. Hu, Z.-G. Zhang, T. Przybilla, G.J. Matt, E. Spiecker, Y. Li, C.J. Brabec, A Universal Interface Layer Based on an Amine-Functionalized Fullerene Derivative with Dual Functionality for Efficient Solution Processed Organic and Perovskite Solar Cells, Adv. Energy Mater. 5 (2015) 1401692. https://doi.org/10.1002/aenm.201401692.

[64]   N.T.P. Hartono, S. Sun, M.C. Gélvez-Rueda, P.J. Pierone, M.P. Erodici, J. Yoo, F. Wei, M. Bawendi, F.C. Grozema, M. Sher, T. Buonassisi, J.-P. Correa-Baena, The effect of structural dimensionality on carrier mobility in lead-halide perovskites, J. Mater. Chem. A. 7 (2019) 23949–23957. https://doi.org/10.1039/C9TA05241K.

[65]   V. Pecunia, Organic Narrowband Photodetectors: Materials, devices and applications, Institute of Physics Publishing, Bristol, UK, 2019.

[66]   A. Baktash, O. Amiri, A. Sasani, Improve efficiency of perovskite solar cells by using Magnesium doped ZnO and TiO 2 compact layers, Superlattices Microstruct. 93 (2016) 128–137. https://doi.org/10.1016/j.spmi.2016.01.026.

[67]   O. Amiri, A.E. Rezaee, H. Teymourinia, M. Salavati-Niasari, L.J. Guo, A. Baktash, New Strategy to Overcome the Instability That Could Speed up the Commercialization of Perovskite Solar Cells, Adv. Mater. Interfaces. 6 (2019) 1900134. https://doi.org/10.1002/admi.201900134.

[68]   M. Mousavi-Kamazani, Z. Zarghami, M. Salavati-Niasari, Facile and Novel Chemical Synthesis, Characterization, and Formation Mechanism of Copper Sulfide (Cu 2 S, Cu 2 S/CuS, CuS) Nanostructures for Increasing the Efficiency of Solar Cells, J. Phys. Chem. C. 120 (2016) 2096–

2108. https://doi.org/10.1021/acs.jpcc.5b11566.

[69]   H. Teymourinia, M. Salavati-Niasari, O. Amiri, M. Farangi, Facile synthesis of graphene quantum dots from corn powder and their application as down conversion effect in quantum dot-dye-sensitized solar cell, J. Mol. Liq. 251 (2018) 267–272. https://doi.org/10.1016/j.molliq.2017.12.059.

[70]   C.W. Kim, W.J. Shin, M.J. Choi, J.H. Lee, S.H. Nam, Y.D. Suh, Y.S. Kang, Y.S. Kang, Wavelength conversion effect-assisted dye-sensitized solar cells for enhanced solar light harvesting, J. Mater. Chem. A. 4 (2016) 11908–11915. https://doi.org/10.1039/C6TA04526J.

Supplementary Material

Enhanced Photoconversion Efficiency in Cesium-Antimony-Halide Perovskite Derivatives by Tuning Crystallographic Dimensionality

Yueheng Peng[a,1], Fengzhu Li[a], Yan Wang[a], Yachen Li[a], Robert L. Z. Hoye[b], Linrun Feng[c], Kai Xia[a], Vincenzo Pecunia[a,1,*]

[a]*Institute of Functional Nano & Soft Materials (FUNSOM), Jiangsu Key Laboratory for Carbon-Based Functional Materials & Devices, Soochow University, 199 Ren'ai Road, Suzhou, 215123, Jiangsu, PR China.*

[b]*Department of Materials, Imperial College London, Exhibition Road, London SW7 2AZ, United Kingdom.*

[c]*Wuhan LinkZill Technology Co., Ltd., Modern Optics Valley World Trade Center, 70 Guanggu Road, Wuhan, 430073, Hubei, China.*

* Corresponding author.

E-mail address: vp293@suda.edu.cn (V. Pecunia)

[1] These authors contributed equally to this work.

.
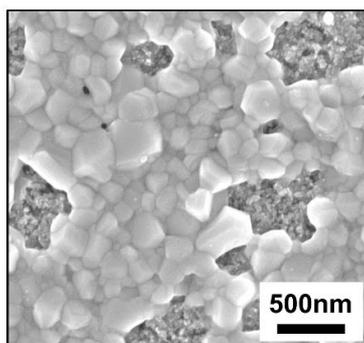
**Fig. S1.** SEM image of solvent-vapor-annealed $Cs_3Sb_2Cl_3I_6$ film on m-TiO_2.
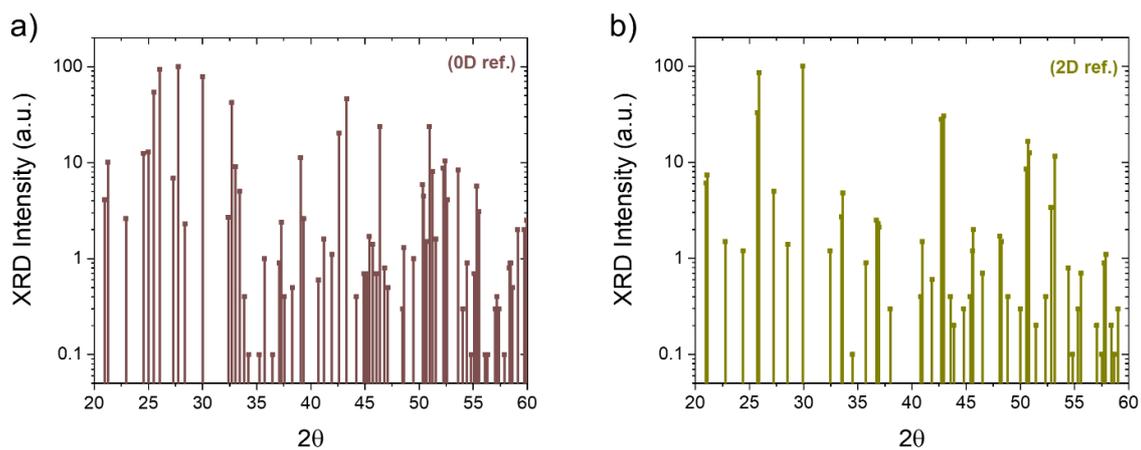
Fig. S2. Reference XRD patterns for a) 0D and b) 2D $Cs_3Sb_2I_9$ [1,2] plotted on a semilogarithmic scale.

| Region no.	Cs	Sb	Cl	I
1	1.67	1	0.88	3.29
2	1.69	1	1.05	3.16
3	1.64	1	1	3.27
Expected	1.5	1	1.5	3
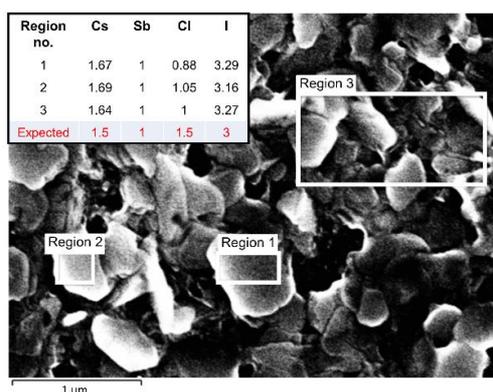
Fig. S3. Elemental mapping of a $Cs_3Sb_2Cl_3I_6$ layer using EDS.
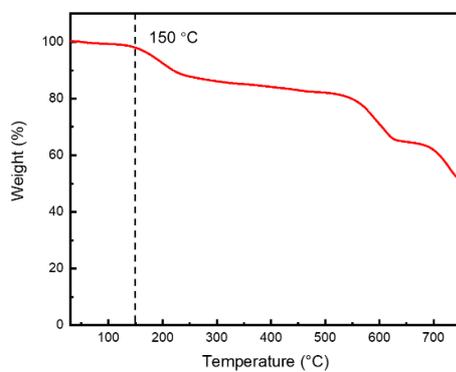
Fig. S4. Thermogravimetric analysis (TGA) of $Cs_3Sb_2Cl_3I_6$.
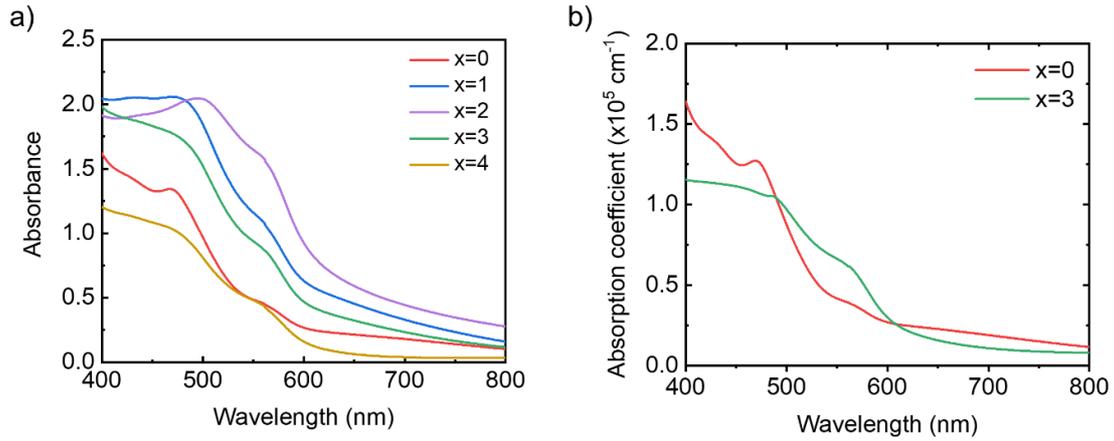
Fig. S5. Optical absorption of $Cs_3Sb_2Cl_xI_{9-x}$ films. a) Absorbance of $Cs_3Sb_2Cl_xI_{9-x}$ films ($x = 0$ – 4, as per precursor mixing ratios) processed via solvent vapor annealing (135 °C) derived from optical transmission experiments. b) Absorption coefficient for $x = 0$ and $x = 3$, calculated from the absorption data as $\alpha = A/(t\log_{10}(e))$, where A is the absorbance and t is the film thickness.
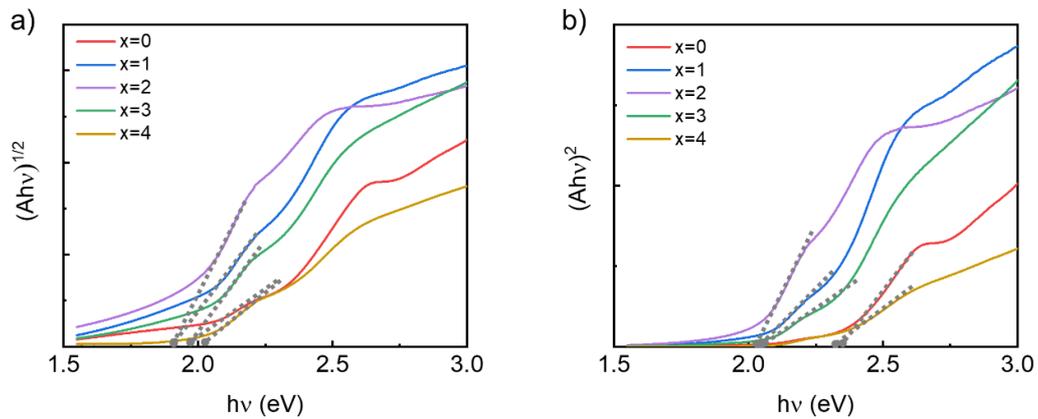

Fig. S6. Tauc analysis of $Cs_3Sb_2Cl_xI_{9-x}$ films. a) Indirect transitions. b) Direct transitions.
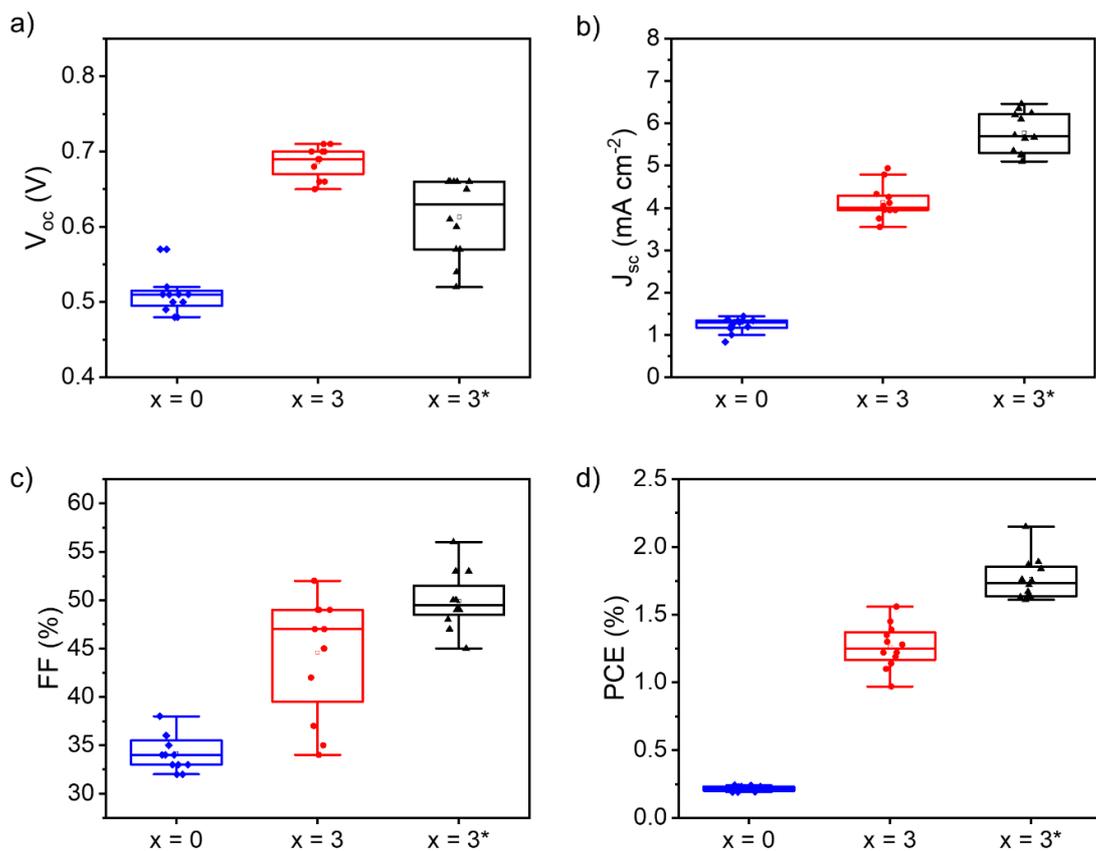
**Fig. S7.** Spread in photovoltaic parameters of $Cs_3Sb_2I_9$ and $Cs_3Sb_2Cl_3I_6$ devices. a) Short-circuit current J_{sc}. b) Open-circuit voltage V_{oc}. c) Fill factor FF. d) Power conversion efficiency PCE. The plots shown in (a-d) refer to $Cs_3Sb_2I_9$ ($x = 0$, poly-TPD), $Cs_3Sb_2Cl_3I_6$ ($x = 3$, poly-TPD), and $Cs_3Sb_2Cl_3I_6$ ($x = 3^*$, LZ-HTL-1-1) devices.
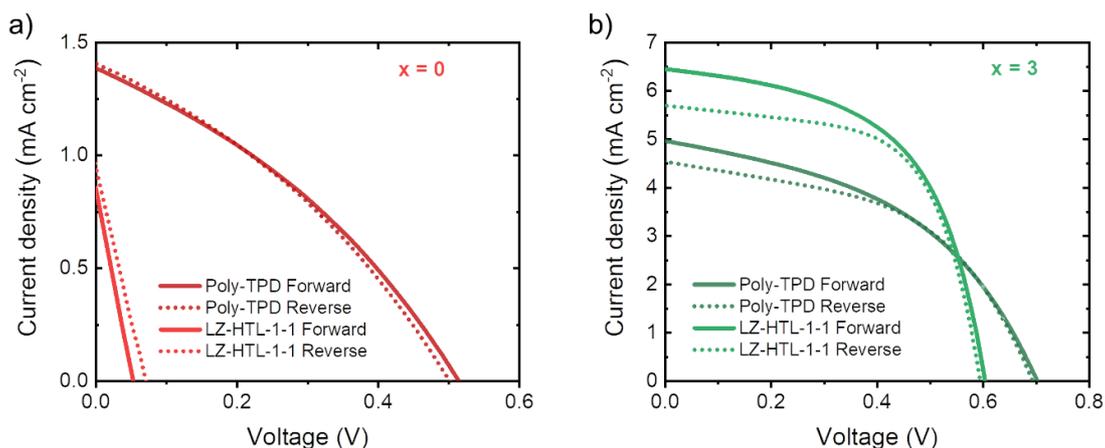
**Fig. S8.** Representative double-sweep current density-voltage characteristics of $Cs_3Sb_2Cl_xI_{9-x}$ devices. a) and b) Double-sweep characteristics under AM 1.5G illumination of $Cs_3Sb_2Cl_xI_{9-x}$ devices on m-TiO$_2$ ($x = 0$ and 3, as per precursor mixing ratios). Characteristics from devices comprising both poly-TPD and LZ-HTL-1-1 as hole transport layers are shown.
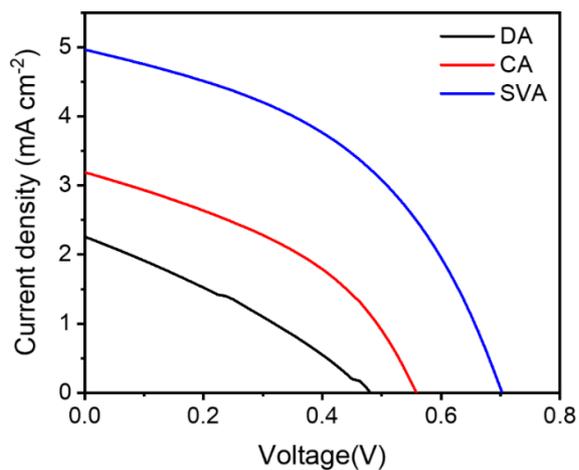
Fig. S9. J-V characteristics of devices comprising $Cs_3Sb_2Cl_3I_6$ layers annealed through the different protocols presented in the main text.
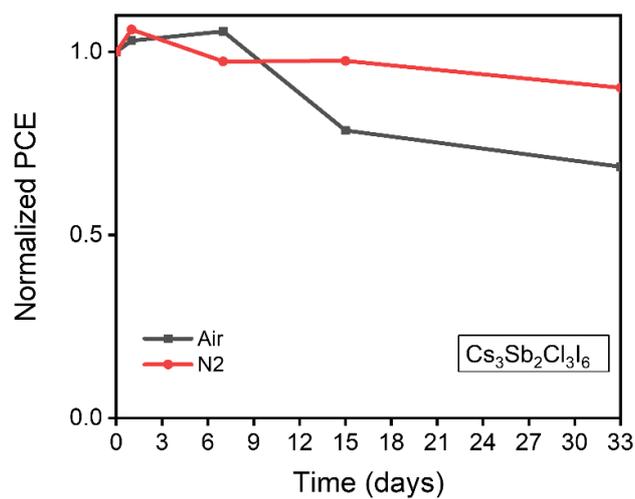
Fig. S10. Stability of non-encapsulated $Cs_3Sb_2Cl_3I_6$ devices stored either in air or in an N_2-filled glove box.
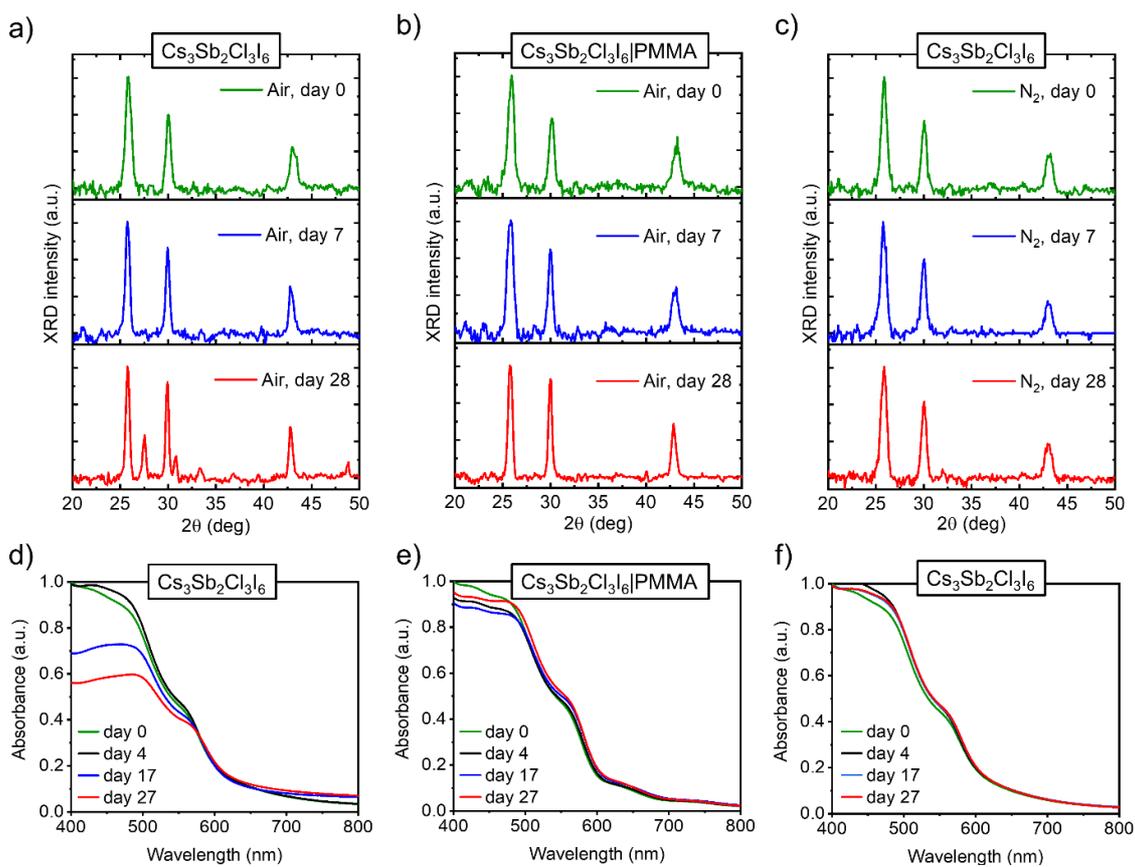
Fig. S11. XRD of $Cs_3Sb_2Cl_3I_6$ films over time: a) sample stored in air; b) sample stored in air and capped with a 400-nm-thick PMMA film; c) sample stored in an N_2-filled glove box. Corresponding UV-Vis absorption spectra are shown in d)-f).
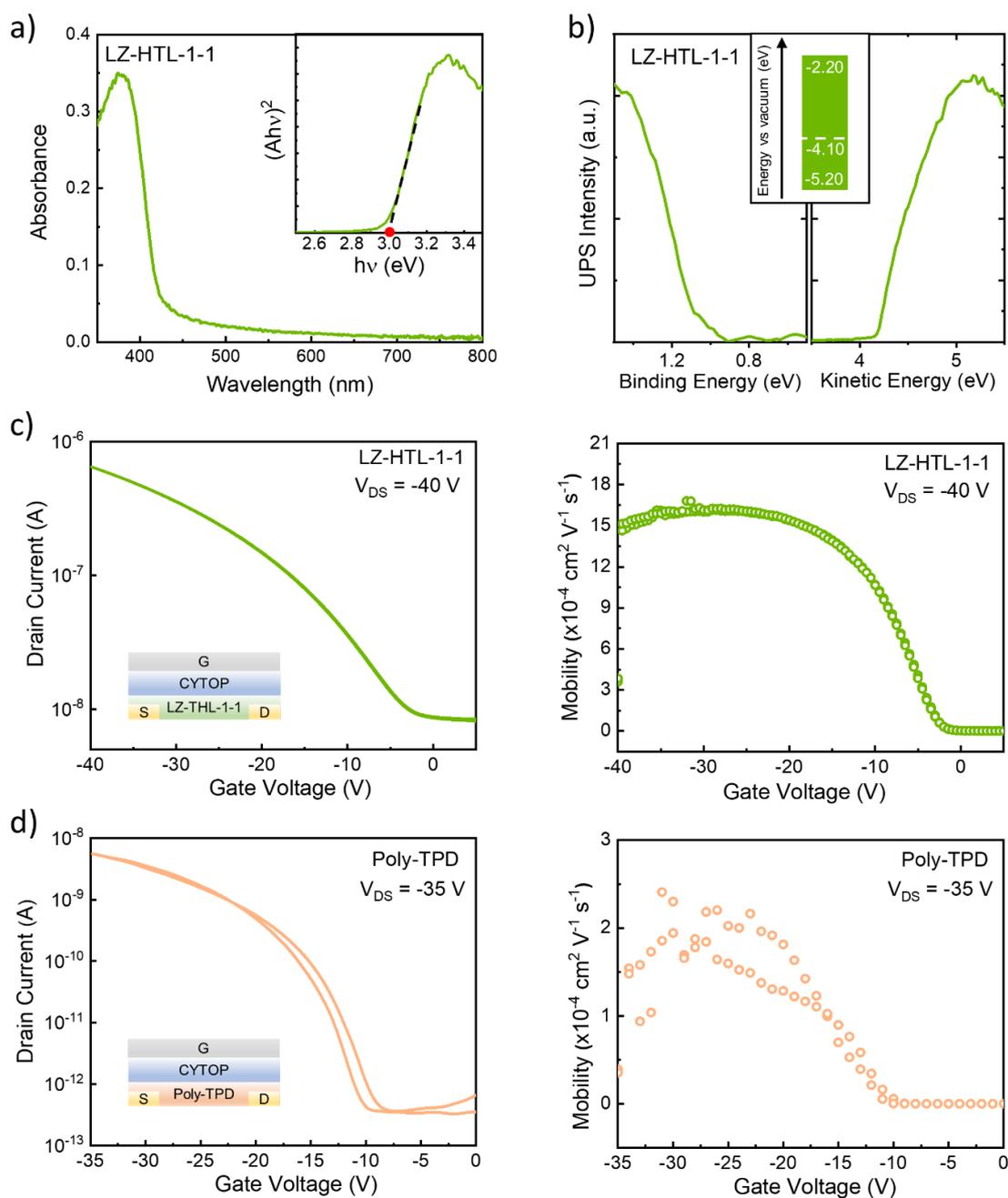
Fig. S12. Energy levels and mobility of LZ-HTL-1-1 hole transport layer. a) Optical absorption spectrum (inset: Tauc plot). b) UPS data (valence band states (left) and He I secondary electron cutoff (right)) (inset: energy diagram under the assumption of negligible excitonic effects). c) Mobility characterization via transistor measurements of the LZ-HTL-1-1 employed as hole transport layer in this study: transfer characteristics (left) (inset: device structure), extracted mobility versus gate voltage (right). d) Mobility characterization via transistor measurements of the poly-TPD employed as hole transport layer in this study: transfer characteristics (left) (inset: device structure), extracted mobility versus voltage (right).
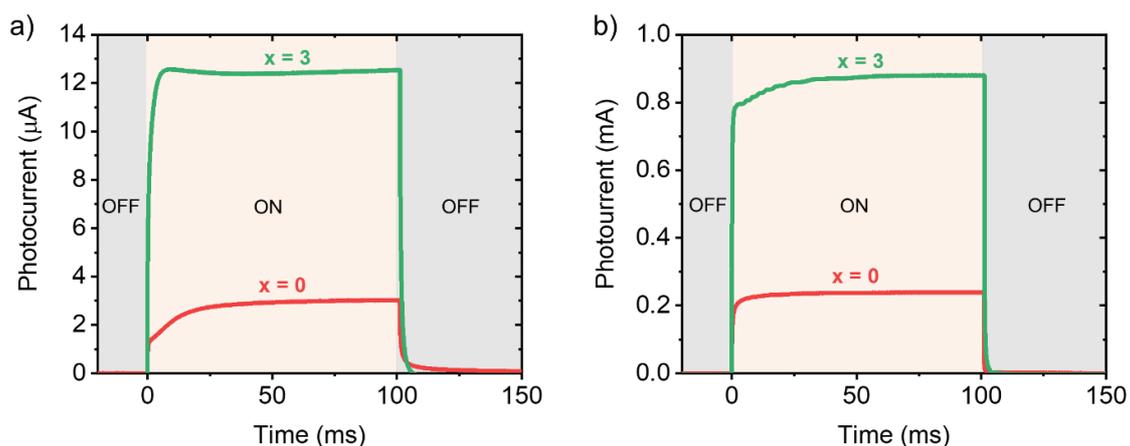
Fig. S13. Representative photocurrent transients of $Cs_3Sb_2Cl_3I_6$ and $Cs_3Sb_2I_9$ devices. Photocurrent transients from $Cs_3Sb_2Cl_3I_6$ and $Cs_3Sb_2I_9$ devices under pulsed illumination (λ = 505 nm) with optical power density equal to a) 1.17 mW cm^{-2} and b) 75.3 mW cm^{-2}.
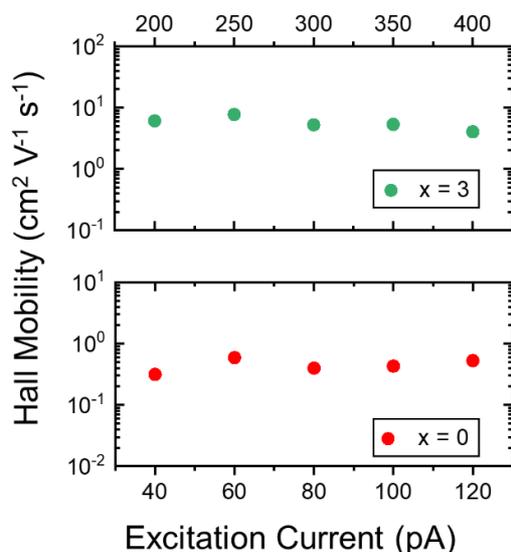
Fig. S14. Hall mobility versus excitation current in $Cs_3Sb_2Cl_3I_6$ and $Cs_3Sb_2I_9$ films. These plots show the Hall mobility values extracted from Hall measurements on $Cs_3Sb_2Cl_3I_6$ and $Cs_3Sb_2I_9$ films in the Van der Pauw configuration. The samples were subjected to an a.c. magnetic field of 0.42291 T modulated at 100 mHz. The resulting Hall mobility values are approximately an invariant of the excitation current, consistently with basic Hall effect theory.

Table S1. EDS compositional analysis of $Cs_3Sb_2Cl_3I_6$ films annealed at different temperatures T_{anneal} (100 °C, 125 °C, and 150 °C).

T_{anneal} = 100 °C					T_{anneal} = 125 °C					T_{anneal} = 150 °C				
No.	Cs	Sb	Cl	I	No.	Cs	Sb	Cl	I	No.	Cs	Sb	Cl	I
Expect.	1.5	1	1.5	3	Expect.	1.5	1	1.5	3	Expect.	1.5	1	1.5	3
1	1.67	1	0.88	3.29	1	1.60	1	0.88	3.02	1	1.67	1	0.78	2.79
2	1.69	1	1.05	3.16	2	1.67	1	0.98	3.32	2	1.71	1	0.95	3.42
3	1.64	1	1	3.27	3	1.67	1	0.96	3.36	3	1.69	1	1.04	3.33

No.: sample number. Expect.: expected.

Table S2. Photovoltaic parameters (best and average) from $Cs_3Sb_2Cl_xI_{9-x}$, x = 1, 2, and 4 (as per precursor mixing ratios) devices employing a poly-TPD HTL. The average values and standard deviations are calculated based on 12 devices of each type.

		V_{oc} (V)	J_{sc} (mA cm^{-2})	FF (%)	PCE (%)
x = 1	Best	0.56	3.87	38	0.82
	Average	0.53 ± 0.05	3.40 ± 0.39	39 ± 1.93	0.71 ± 0.12
x = 2	Best	0.60	5.46	45	1.48
	Average	0.59 ± 0.01	4.79 ± 0.38	43 ± 2.57	1.22 ± 0.13
x = 4	Best	0.59	3.82	49	1.12
	Average	0.60 ± 0.01	3.20 ± 0.49	48 ± 2.35	0.92 ± 0.15

Table S3. Photovoltaic parameters of literature implementations of Sb- and Bi-halide perovskite derivatives.

Ref.	Active layer	V_{oc} [V]	J_{sc} [mA cm^{-2}]	FF [%]	PCE [%]	EQE_{max} [%]
Hebig et al.[3]	$MA_3Sb_2I_9$	0.90	1.00	55	0.49	13
Boopathi et al.[4]	$MA_3Sb_2I_9$	0.62	5.41	61	2.04	21
Karuppuswamy et al.[5]	$MA_3Sb_2I_9$	0.70	6.64	60	2.77	26
Jiang et al.[6]	$MA_3Sb_2Cl_xI_{9-x}$	0.69	5.04	0.63	2.19	65
Saparov et al.[7]	$Cs_3Sb_2I_9$	≈ 0.30	≈ 0.05	≈ 34	≈ 0.005	-
Boopathi et al.[4]	$Cs_3Sb_2I_9$	0.60	2.91	48	0.84	18
Singh et al.[8]	$Cs_3Sb_2I_9$	0.68	5.31	39	1.49	39
Umar et al.[9]	$Cs_3Sb_2I_9$	0.61	3.55	55.85	1.21	32
Harikesh et al.[10]	$Rb_3Sb_2I_9$	0.55	2.11	56.97	0.66	32.8
Correa-Baena et al.[11]	$Rb_3Sb_2I_9$	0.66	1.84	63	0.76	-
Weber et al.[12]	$Rb_3Sb_2Br_{9-x}I_x$	0.55	4.25	59.56	1.37	26.7
Correa-Baena et al.[11]	$K_3Sb_2I_9$	0.34	0.41	50	0.07	-
Ran et al.[13]	$MA_3Bi_2I_9$	0.83	1.39	34	0.39	23
Jain et al.[14]	$MA_3Bi_2I_9$	1.01	4.02	78	3.17	48
Zhang et al.[15]	$MA_3Bi_2I_9$	0.67	1.00	60	0.42	25
Mali et al.[16]	$MA_3Bi_2I_9$	0.65	1.1	50	0.36	-
Kulkarni et al.[17]	$MA_3Bi_2I_9$	0.51	0.94	61	0.31	28
Singh et al.[18]	$MA_3Bi_2I_9$	0.56	0.83	49	0.26	4.6
Park et al.[19]	$MA_3Bi_2I_9$	0.68	0.52	33	0.12	12
Abulikemu et al.[20]	$MA_3Bi_2I_9$	0.72	0.49	32	0.11	17
Lyu et al.[21]	$MA_3Bi_2I_9$	0.35	1.16	0.46	0.19	22
Öz et al.[22]	$MA_3Bi_2I_9$	0.66	0.22	0.49	0.07	-
Li et al.[23]	$MA_3Bi_2I_9$	0.84	0.17	35	0.05	4.0
Zhang et al.[24]	$MA_3Bi_2I_9$	0.83	3.00	79	1.64	60
Jain et al.[25]	$MA_3Bi_2I_9$	0.87	2.7	69	1.62	25
Park et al.[19]	$MA_3Bi_2I_9Cl_x$	0.04	0.18	0.38	0.003	-
Johansson et al.[26]	$Cs_3Bi_2I_9$	0.31	3.4	38	0.4	25
Park et al.[19]	$Cs_3Bi_2I_9$	0.85	2.15	60	1.09	-
Bai et al.[27]	$Cs_3Bi_2I_9$	0.86	5.78	64	3.2	56
Yu et al.[28]	$Cs_3Bi_2Br_xI_{9-x}$	0.64	3.15	57	1.15	32
Li et al.[29]	$C_5H_6NBiI_4$	0.62	2.71	54	0.9	-
Li et al.[30]	$(C_6H_5NH_3)BiI_4$	0.58	6.03	22	0.78	-

Table S4. Parameters derived from Hall effect experiments on $Cs_3Sb_2Cl_3I_6$ and $Cs_3Sb_2I_9$ films in the Van der Pauw configuration. Samples were subjected to an a.c. magnetic field of 0.42291 T modulated at 100 mHz.

$Cs_3Sb_2I_9$					$Cs_3Sb_2Cl_3I_6$				
Current (pA)	Resistivity [MΩ·cm]	μ_H [10^{-1} cm²V⁻¹s⁻¹]	Carrier Conc. [10^{12}/cm³]	Hall Voltage [μV]	Current (pA)	Resistivity [MΩ·cm]	μ_H [cm²V⁻¹s⁻¹]	Carrier Conc. [10^{11}/cm³]	Hall Voltage [mV]
40	7.16	3.14	2.77	71	200	1.64	6.07	6.26	2.41
60	7.58	5.91	1.39	214	250	1.58	7.74	5.10	3.77
80	8.12	3.97	1.93	203	300	1.51	5.22	8.07	2.94
100	8.54	4.29	1.69	274	350	1.45	5.32	7.88	3.34
120	8.78	5.26	1.35	398	400	1.35	4.02	9.62	3.20

Supplementary references

[1] B. Chabot, E. Parthé, Cs 3 Sb 2 I 9 and Cs 3 Bi 2 I 9 with the hexagonal Cs 3 Cr 2 Cl 9 structure type, Acta Crystallogr. Sect. B Struct. Crystallogr. Cryst. Chem. 34 (1978) 645–648. https://doi.org/10.1107/S0567740878003684.

[2] K. Yamada, H. Sera, S. Sawada, H. Tada, T. Okuda, H. Tanaka, Reconstructive Phase Transformation and Kinetics of Cs3Sb2I9 by Means of Rietveld Analysis of X-Ray Diffraction and 127I NQR, J. Solid State Chem. 134 (1997) 319–325. https://doi.org/10.1006/jssc.1997.7562.

[3] J.-C. Hebig, I. Kühn, J. Flohre, T. Kirchartz, Optoelectronic Properties of (CH 3 NH 3) 3 Sb 2 I 9 Thin Films for Photovoltaic Applications, ACS Energy Lett. 1 (2016) 309–314. https://doi.org/10.1021/acsenergylett.6b00170.

[4] K.M. Boopathi, P. Karuppuswamy, A. Singh, C. Hanmandlu, L. Lin, S.A. Abbas, C.C. Chang, P.C. Wang, G. Li, C.W. Chu, Solution-processable antimony-based light-absorbing materials beyond lead halide perovskites, J. Mater. Chem. A. 5 (2017) 20843–20850. https://doi.org/10.1039/C7TA06679A.

[5] P. Karuppuswamy, K.M. Boopathi, A. Mohapatra, H.-C. Chen, K.-T. Wong, P.-C. Wang, C.-W. Chu, Role of a hydrophobic scaffold in controlling the crystallization of methylammonium antimony iodide for efficient lead-free perovskite solar cells, Nano Energy. 45 (2018) 330–336. https://doi.org/10.1016/j.nanoen.2017.12.051.

[6] F. Jiang, D. Yang, Y. Jiang, T. Liu, X. Zhao, Y. Ming, B. Luo, F. Qin, J. Fan, H. Han, L. Zhang, Y. Zhou, Chlorine-Incorporation-Induced Formation of the Layered Phase for Antimony-Based Lead-Free Perovskite Solar Cells, J. Am. Chem. Soc. 140 (2018) 1019–1027. https://doi.org/10.1021/jacs.7b10739.

[7] B. Saparov, F. Hong, J.-P. Sun, H.-S. Duan, W. Meng, S. Cameron, I.G. Hill, Y. Yan, D.B. Mitzi, 5, Chem. Mater. 27 (2015) 5622–5632. https://doi.org/10.1021/acs.chemmater.5b01989.

[8] A. Singh, K.M. Boopathi, A. Mohapatra, Y.F. Chen, G. Li, C.W. Chu, 6, ACS Appl. Mater. Interfaces. 10 (2018) 2566–2573. https://doi.org/10.1021/acsami.7b16349.

[9] F. Umar, J. Zhang, Z. Jin, I. Muhammad, X. Yang, H. Deng, K. Jahangeer, Q. Hu, H. Song, J. Tang, 7, Adv. Opt. Mater. 7 (2019) 1801368. https://doi.org/10.1002/adom.201801368.

[10] P.C. Harikesh, H.K. Mulmudi, B. Ghosh, T.W. Goh, Y.T. Teng, S. Mhaisalkar, N. Mathews, 8, (2016). https://doi.org/10.1021/acs.chemmater.6b03310.

[11] J.-P. Correa-Baena, L. Nienhaus, R.C. Kurchin, S.S. Shin, S. Wieghold, N.T. Putri Hartono, M. Layurova, N.D. Klein, J.R. Poindexter, A. Polizzotti, S. Sun, M.G. Bawendi, T. Buonassisi, A-Site Cation in Inorganic A3Sb2I9 Perovskite Influences Structural Dimensionality, Exciton Binding Energy, and Solar Cell Performance, Chem. Mater. 30 (2018) 3734–3742. https://doi.org/10.1021/acs.chemmater.8b00676.

[12] S. Weber, T. Rath, K. Fellner, R.C. Fischer, R. Resel, B. Kunert, T. Dimopoulos, A. Steinegger, G. Trimmel, 10, (2018). https://doi.org/10.1021/acsaem.8b01572.

[13] C. Ran, Z. Wu, J. Xi, F. Yuan, H. Dong, T. Lei, X. He, X. Hou, Construction of Compact Methylammonium Bismuth Iodide Film Promoting Lead-Free Inverted Planar Heterojunction Organohalide Solar Cells with Open-Circuit Voltage over 0.8 V, J. Phys. Chem. Lett. 8 (2017) 394–400. https://doi.org/10.1021/acs.jpclett.6b02578.

[14] S.M. Jain, D. Phuyal, M.L. Davies, M. Li, B. Philippe, C. De Castro, Z. Qiu, J. Kim, T. Watson, W.C. Tsoi, O. Karis, H. Rensmo, G. Boschloo, T. Edvinsson, J.R. Durrant, An effective approach of vapour assisted morphological tailoring for reducing metal defect sites in lead-free, (CH3NH3)3Bi2I9 bismuth-based perovskite solar cells for improved performance and long-term stability, Nano Energy. 49 (2018) 614–624. https://doi.org/10.1016/j.nanoen.2018.05.003.

[15] X. Zhang, G. Wu, Z. Gu, B. Guo, W. Liu, S. Yang, T. Ye, C. Chen, W. Tu, H. Chen, Active-layer evolution and efficiency improvement of (CH3NH3 3Bi2I9-based solar cell on TiO2-deposited ITO substrate, Nano Res. 9 (2016) 2921–2930. https://doi.org/10.1007/s12274-016-1177-8.

[16] S.S. Mali, H. Kim, D.-H. Kim, C. Kook Hong, Anti-Solvent Assisted Crystallization Processed Methylammonium Bismuth Iodide Cuboids towards Highly Stable Lead-Free Perovskite Solar Cells, ChemistrySelect. 2 (2017) 1578–1585. https://doi.org/10.1002/slct.201700025.

[17] A. Kulkarni, T. Singh, M. Ikegami, T. Miyasaka, Photovoltaic enhancement of bismuth halide hybrid perovskite by N-methyl pyrrolidone-assisted morphology conversion, RSC Adv. 7 (2017) 9456–9460. https://doi.org/10.1039/C6RA28190G.

[18] T. Singh, A. Kulkarni, M. Ikegami, T. Miyasaka, Effect of Electron Transporting Layer on Bismuth-Based Lead-Free Perovskite (CH 3 NH 3) 3 Bi 2 I 9 for Photovoltaic Applications, ACS Appl. Mater. Interfaces. 8 (2016) 14542–14547. https://doi.org/10.1021/acsami.6b02843.

[19] B.W. Park, B. Philippe, X. Zhang, H. Rensmo, G. Boschloo, E.M.J. Johansson, Bismuth Based Hybrid Perovskites A3Bi2I9 (A: Methylammonium or Cesium) for Solar Cell Application, Adv. Mater. 27 (2015) 6806–6813. https://doi.org/10.1002/adma.201501978.

[20] M. Abulikemu, S. Ould-Chikh, X. Miao, E. Alarousu, B. Murali, G.O. Ngongang Ndjawa, J. Barbé, A. El Labban, A. Amassian, S. Del Gobbo, Optoelectronic and photovoltaic properties of the air-stable organohalide semiconductor (CH 3 NH 3) 3 Bi 2 I 9, J. Mater. Chem. A. 4 (2016) 12504–12515. https://doi.org/10.1039/C6TA04657F.

[21] M. Lyu, J.H. Yun, M. Cai, Y. Jiao, P. V. Bernhardt, M. Zhang, Q. Wang, A. Du, H. Wang, G. Liu, L. Wang, Organic-inorganic bismuth (III)-based material: A lead-free, air-stable and solution-processable light-absorber beyond organolead perovskites, Nano

Res. 9 (2016) 692–702. https://doi.org/10.1007/s12274-015-0948-y.

[22]   S. Öz, J.C. Hebig, E. Jung, T. Singh, A. Lepcha, S. Olthof, F. Jan, Y. Gao, R. German, P.H.M. van Loosdrecht, K. Meerholz, T. Kirchartz, S. Mathur, Zero-dimensional (CH3NH3)3Bi2I9 perovskite for optoelectronic applications, Sol. Energy Mater. Sol. Cells. 158 (2015) 195–201. https://doi.org/10.1016/j.solmat.2016.01.035.

[23]   H. Li, C. Wu, Y. Yan, B. Chi, J. Pu, J. Li, S. Priya, Fabrication of Lead-Free (CH 3 NH 3) 3 Bi 2 I 9 Perovskite Photovoltaics in Ethanol Solvent, ChemSusChem. 10 (2017) 3994–3998. https://doi.org/10.1002/cssc.201701470.

[24]   Z. Zhang, X. Li, X. Xia, Z. Wang, Z. Huang, B. Lei, Y. Gao, High-Quality (CH 3 NH 3) 3 Bi 2 I 9 Film-Based Solar Cells: Pushing Efficiency up to 1.64%, J. Phys. Chem. Lett. 8 (2017) 4300–4307. https://doi.org/10.1021/acs.jpclett.7b01952.

[25]   S.M. Jain, T. Edvinsson, J.R. Durrant, Green fabrication of stable lead-free bismuth based perovskite solar cells using a non-toxic solvent, Commun. Chem. 2 (2019) 91. https://doi.org/10.1038/s42004-019-0195-3.

[26]   M.B. Johansson, H. Zhu, E.M.J. Johansson, Extended Photo-Conversion Spectrum in Low-Toxic Bismuth Halide Perovskite Solar Cells, J. Phys. Chem. Lett. 7 (2016) 3467–3471. https://doi.org/10.1021/acs.jpclett.6b01452.

[27]   F. Bai, Y. Hu, Y. Hu, T. Qiu, X. Miao, S. Zhang, Lead-free, air-stable ultrathin Cs3Bi2I9 perovskite nanosheets for solar cells, Sol. Energy Mater. Sol. Cells. 184 (2018) 15–21. https://doi.org/10.1016/j.solmat.2018.04.032.

[28]   B.-B. Yu, M. Liao, J. Yang, W. Chen, Y. Zhu, X. Zhang, T. Duan, W. Yao, S.-H. Wei, Z. He, 26, J. Mater. Chem. A. 7 (2019) 8818–8825. https://doi.org/10.1039/C9TA01978B.

[29]   T. Li, Y. Hu, C.A. Morrison, W. Wu, H. Han, N. Robertson, Lead-free pseudo-three-dimensional organic–inorganic iodobismuthates for photovoltaic applications, Sustain. Energy Fuels. 1 (2017) 308–316. https://doi.org/10.1039/C6SE00061D.

[30]   X.-L. Li, L.-L. Gao, B. Ding, Q.-Q. Chu, Z. Li, G.-J. Yang, (C 6 H 5 NH 3)BiI 4 : a lead-free perovskite with >330 days humidity stability for optoelectronic applications, J. Mater. Chem. A. 7 (2019) 15722–15730. https://doi.org/10.1039/C9TA02421B.